




Vortex-induced vibration of a slender flexible riser with grooved and spanwise strips subject to uniform currents

Cite as: Phys. Fluids **34**, 125131 (2022); <https://doi.org/10.1063/5.0129218>

Submitted: 04 October 2022 • Accepted: 30 November 2022 • Published Online: 19 December 2022

 Hao Hu (胡浩),  Weiwen Zhao (赵伟文) and  Decheng Wan (万德成)



View Online



Export Citation



CrossMark

ARTICLES YOU MAY BE INTERESTED IN

[Numerical investigations of the flow-induced vibration of a three-dimensional circular cylinder with various symmetric strips attached](#)

Phys. Fluids **34**, 065102 (2022); <https://doi.org/10.1063/5.0087312>

[Control of vortex-induced vibration of an elastically mounted cylinder with a pair of porous rods](#)

Phys. Fluids **34**, 123610 (2022); <https://doi.org/10.1063/5.0131282>

[Reconstructing turbulent velocity information for arbitrarily gappy flow fields using the deep convolutional neural network](#)

Phys. Fluids **34**, 127117 (2022); <https://doi.org/10.1063/5.0130955>



Physics of Fluids

Special Topic: Paint and Coating Physics

Submit Today!

Vortex-induced vibration of a slender flexible riser with grooved and spanwise strips subject to uniform currents

Cite as: Phys. Fluids **34**, 125131 (2022); doi: [10.1063/5.0129218](https://doi.org/10.1063/5.0129218)
Submitted: 4 October 2022 · Accepted: 30 November 2022 ·
Published Online: 19 December 2022



Hao Hu (胡浩), Weiwen Zhao (赵伟文), and Decheng Wan (万德成)^{a)}

AFFILIATIONS

Computational Marine Hydrodynamics Lab (CMHL), School of Naval Architecture, Ocean and Civil Engineering, Shanghai Jiao Tong University, Shanghai 200240, China

^{a)} Author to whom correspondence should be addressed: dcwan@sjtu.edu.cn

ABSTRACT

We report a numerical investigation of the suppression of “vortex-induced vibration” (VIV) of a cylindrical flexible riser to which are attached various grooved or strip configurations with the ensemble exposed to uniform flow. Based on the thick-strip model, the simulation is done using our in-house three-dimensional VIV solver based on the Open Field Operation and Manipulation toolbox and developed at Shanghai Jiao Tong University (referred to as “viv3D-FOAM-SJTU”). The solver is applied to calculate all the simulations; it uses the Navier–Stokes equations to calculate flow field and the Euler–Bernoulli bending-beam hypothesis to calculate the vibrational displacements of the riser. A slender flexible riser with two spanwise symmetrical strips is first used to determine the appropriate installation angle of the strips, and cylindrical or grooved risers with different strip configurations are used to improve VIV suppression. The numerical results show that the spanwise strip installation angles of 30° and 45° suppress VIV due to the secondary separation of the boundary layer, but suffer from higher crossflow vibration frequency, which brings the risk of inducing high-order mode vibration, the enhancement of the lift correlation along the spanwise direction, and the increment of total drag. The main function of spanwise strips installed at 135° and 150° is to divide the wake region, which also helps suppress VIV. The introduction of grooves in the riser combined with strips of suitable thickness reduces the correlation of lift along the span, which in turn reduces crossflow vibration frequency and the total drag, and enhances VIV suppression. Of all the configurations, the grooved riser with four staggered symmetrical strips most strongly suppresses VIV in the crossflow direction.

Published under an exclusive license by AIP Publishing. <https://doi.org/10.1063/5.0129218>

I. INTRODUCTION

Fundamental research on cylinders exposed to uniform flow shows that, when the Reynolds number $Re = UD/\nu > 40$,¹ periodic positive and negative vortices are released into the wake region of the cylinder and form the Bénard–von Kármán vortex street. Upon further increasing the Reynolds number, the wake region goes from laminar flow to turbulent flow. As a result, vortex shedding produces periodic pressure differential forces that act on the cylinder surface in the crossflow and inline directions. These are called “lift” and “drag,” respectively, and induce crossflow and inline vibrations of the cylinder, respectively, which are called vortex-induced vibrations (VIVs). In addition, VIVs of the cylinder are amplified when the vortex-shedding frequency is in phase with the natural vibration frequency of the structure, a phenomenon called “lock-in.”

Given that long flexible cylindrical risers are commonly applied to transport oil and gas from the seabed in ocean engineering, research

on VIVs of circular cross-section risers has drawn considerable attention in the last two decades.^{2–5} Cylindrical risers are also used as references for other VIV studies of risers with modified cross sections. To avoid fatigue damage of marine risers and enhance the safety of oil and gas transportation, which is affected by the significant deflection of marine risers caused by VIV, controlling VIV has been a goal of numerous research efforts over the years. For a broad review of VIV-suppression strategies, please see Refs. 6–8.

Strategies to control VIV may be classified as active (i.e., with additional energy input) or passive (i.e., with no energy input). The main advantage of active control strategies is that the adjustable power input can handle a sophisticated incident-flow environment, allowing VIVs to be easily and precisely controlled. The plasma actuators⁹ generate a wall jet through ion release to control the VIV, but it requires stable high-voltage power supply control and reliable circuit design. The synthetic jets¹⁰ control the VIV through the “blowing and

suction” fluid, but it requires expensive materials to ensure the strength of the structure. The heating cylinder¹¹ interferes with the flow field through the temperature difference to control the VIV, but it requires an accurate temperature control device. Similarly, the rotating control rods¹² control the vortex-induced vibration by destroying the wake region, but it also requires an accurate speed control system. Therefore, using these devices usually incurs additional economic and technical costs, which hinders their wide application.

Passive VIV-control strategies mainly modify the geometry of the bluff body, facilitating their machining and making them more attractive in engineering. Conventional passive VIV-control devices are subdivided into two categories: The first category introduces extra geometry on or around the cylinder surface. The splitter plate is a structure proposed by Roshko¹³ that controls VIV by separating the upper wake region from the lower. In recent decades, researchers have also investigated splitter plates, such as flexible splitter plates, double-tail splitter plates with different angles, and parallel and C-shaped splitter plates.^{14–16} Splitter plates have also been streamlined by using a device called a “fairing.” Assi *et al.*¹⁷ compared the capacity of short-tailed fairings and splitter plates to suppress VIVs and reported that the former eliminates galloping vibration in splitter plates. Zhu *et al.*¹⁸ numerically studied the free-to-rotate triangular fairing and found that the tip angle plays an important role in VIV suppression. Wang *et al.*¹⁹ investigated the VIV response to triangular, trapezoidal, and rectangular fairings. Their results show that the rectangular fairing has the best suppression effect but is accompanied by the maximum resistance rise. To improve the robustness of passive VIV suppression devices in a complex incident-flow environment, researchers have fixed bumps to the entire cylinder surface.^{20–22} Furthermore, leveraging the merits of the splitter plate are helical strakes, which have seen significant use. Quen *et al.*²³ reported the VIV suppression for helical strakes with different starts, heights (h), and pitches (p). Their results show that a riser with three-start helical strakes of $p = 10D$ and $h = 0.15D$ (where D is the riser outer diameter) performs the best. Ishihara and Li²⁴ used the large-eddy simulation (LES) turbulence model to simulate VIVs on a cylinder with helical wires. The numerical results indicate that the helical wires decrease the lift, whereas the magnitude of the drag on a wired cylinder remains the same as that on a bare cylinder. Ma *et al.*²⁵ experimentally investigated VIV control by using a flexible helical strake riser with time-varying axial tension. They reported that axial excitation caused by time-varying axial tension hinders VIV suppression by a helical strake.

Given the risk of increasing the mean drag force by installing additional geometries, the second category of passive VIV-control strategies concentrates on modifying the circular cross section of the cylinder. Baek and Karniadakis²⁶ made a slit parallel to the current in the cylinder cross section, which was shown by numerical methods to reduce displacement by over 70% in the y direction. Wang *et al.*²⁷ introduced a bionic-cactus cross section to control VIV and found that the flow separation point is altered by this cross-sectional structure, which suppresses VIV. Huang²⁸ added three-start helical grooves to a cylinder, which experimentally reduced the drag coefficient and VIV amplitude by 25% and 64%, respectively. Law and Jaiman²⁹ numerically analyzed VIV for a staggered groove and a helical groove, and report that the staggered groove better suppresses VIV (up to 37% and 25% reduction in cross-flow amplitude and in the drag coefficient, respectively). Zhao *et al.*³⁰ investigated the VIV of cylinders with

symmetrical grooves by varying the angle between the grooves and the incident flow and found that, at certain angles, symmetrical grooves are better for controlling VIV.

The above introduction shows that the research on VIV suppression has significant progress. However, as a slender structure, when the widely used passive suppression devices such as splitter plates, fairings, and helical strakes are installed on the surface of the riser, the manufacturing cost is still high. Based on the study of Ma *et al.*^{31,32} for stationary rigid cylinders, the spanwise symmetrical strips be used as a passive control device with higher simplicity, adjustability, and ease of operation on cylindrical surfaces, bringing a low cost. Therefore, the present work first considers flexible cylindrical risers with two spanwise symmetrical strips attached. Combining the advantages of the method of modifying the circular cross section, we also propose the use of flexible risers with grooves and strips to better suppress VIV. Although numerical investigations of slender flexible risers have received increasing attention, a few such studies consider the large aspect ratio of marine risers of the 3D effect of flow around such risers. Simulations of the VIV of flexible cylindrical and grooved risers with symmetrical strips attached are implemented by our in-house viv3D-FOAM-SJTU software based on the thick-strip model and Open Field Operation and Manipulation software to explore the physical mechanisms by which the riser surface structure perturbs the 3D flow field around it. This software was developed and verified by Deng *et al.*^{33,34} The objectives of this article are as follows:

- (1) To suppress VIV, this study considers how structural vibration is affected by the position of two symmetrical spanwise strips fixed to the riser surface, and figures out the physical mechanism of suppressing or enhancing VIV by the 3D flow-field analysis.
- (2) To suppress VIV in flexible risers, we seek to understand how vibration is induced by various groove and strip configurations, and explore in detail the physical mechanism of VIV suppression by the 3D flow-field analysis.
- (3) Finally, the numerical results reported here can be used as a reference; for example, to suppress VIV in a slender flexible riser in oscillatory flow, or in two or more slender flexible risers in tandem.

The remainder of this paper is structured as follows: Section II introduces the hydrodynamic and structural numerical methods and the thick-strip model for dealing with flow fields. Section III describes the configurations, mesh details, and boundary conditions for all simulations. Section IV validates the reliability and convergence of the numerical calculation for the Reynolds number $Re = 4000$. Section V gives the numerical results for $\alpha = 30^\circ, 45^\circ, 60^\circ, 120^\circ, 135^\circ,$ and 150° , where α is the angle between the strip’s geometric central line and the stagnation point in front of the riser. Section VI compares the numerical VIV suppression results for six different configurations (with the strip thickness in each configuration taking on two values, $t_s = 0.05D$ and $0.08D$). Finally, Sec. VII summarizes the simulation results.

II. NUMERICAL METHOD

A. Hydrodynamic governing equations

In this study, the flow field around the riser is governed by the incompressible viscous Navier–Stokes equations, including the continuity equation and the momentum equation,

$$\frac{\partial u_i}{\partial x_i} = 0, \tag{1}$$

$$\frac{\partial u_i}{\partial t} + \frac{\partial u_i u_j}{\partial x_j} = -\frac{1}{\rho} \frac{\partial p}{\partial x_i} + \frac{\partial}{\partial x_j} \left[\nu \left(\frac{\partial u_i}{\partial x_j} + \frac{\partial u_j}{\partial x_i} \right) \right], \tag{2}$$

where ρ is the fluid density, u is the fluid velocity, p is the fluid pressure, ν is the kinematic viscosity of the fluid, and $i, j = 1, 2, 3$ are the components of the physical quantity in a Cartesian coordinate system.

Our goal is to capture the small-scale eddy structures formed by the complex cross section of a flexible riser in large-separation flow of VIV. The shear stress transport k - ω turbulence-delayed detached eddy simulation (SST-DDES) model,³⁵ which simultaneously combines the advantages of the Reynolds-averaged Navier–Stokes (RANS) model and a large-eddy simulation (LES) model, is used to close the momentum equation. For the near-wall calculation, the SST-DDES model uses the SST k - ω model, and the large-eddy simulation sub-grid model is dominant when the numerical calculation addresses the separated-flow region. The blending length, which serves as a decision criterion for the conversion between these two models, is modified by a delay function to prevent premature separation of boundary layers caused by premature conversion of either model. Therefore, the final transport equations for turbulence kinetic energy k and turbulence dissipation rate ω are as follows:

$$\frac{\partial k}{\partial t} + \frac{\partial (u_j k)}{\partial x_j} = \tilde{G} - \frac{k^{3/2}}{l} + \frac{\partial}{\partial x_j} \left[(\nu + \alpha_k \nu_t) \frac{\partial k}{\partial x_j} \right], \tag{3}$$

$$\begin{aligned} \frac{\partial \omega}{\partial t} + \frac{\partial (u_j \omega)}{\partial x_j} = & \frac{c}{\nu_t} \tilde{G} - \beta \omega^2 + \frac{\partial}{\partial x_j} \left[(\nu + \alpha_\omega \nu_t) \frac{\partial \omega}{\partial x_j} \right] \\ & + 2(1 - I_1) \frac{\alpha_{\omega 2}}{\omega} \frac{\partial k}{\partial x_j} \frac{\partial \omega}{\partial x_j}, \end{aligned} \tag{4}$$

where \tilde{G} is the turbulence kinetic energy production term, $\tilde{G} = \min(\nu_t S^2, 10 \cdot C_\mu k \omega)$, l is the DDES turbulence length scale, which is defined by Gritskevich *et al.*,³⁵ $\nu_t = \frac{a_1 k}{\max(a_1 \omega, I_2 S)}$ is the turbulent eddy viscosity S is the invariant strain rate, I_1 and I_2 are the first and second SST blending functions,³⁶ and $\alpha_k, c, \beta, \alpha_\omega, \alpha_{\omega 2}, C_\mu,$ and a_1 , are the fixed values proposed by Gritskevich *et al.* and Menter *et al.*^{35,36}

B. Structural governing equations

This study considers a marine riser as a slender rod structure under axial pretension with two ends simply supported, which is consistent with the hypothesis of the Bernoulli–Euler bending-beam model. In addition, the material is homogeneous along the riser span, neglecting the torsional deformation and axial tension deformation of the structure. The vibration differential equations describing each discrete structural element of the riser as a function of time are as follows:

$$\begin{aligned} EI \frac{\partial^4}{\partial z^4} x(z, t) - \frac{\partial}{\partial z} \left[T(z) \frac{\partial x(z, t)}{\partial z} \right] + m \frac{\partial^2 x(z, t)}{\partial t^2} + c \frac{\partial x(z, t)}{\partial t} \\ = F_x(z, t), \end{aligned} \tag{5}$$

$$\begin{aligned} EI \frac{\partial^4}{\partial z^4} y(z, t) - \frac{\partial}{\partial z} \left[T(z) \frac{\partial y(z, t)}{\partial z} \right] + m \frac{\partial^2 y(z, t)}{\partial t^2} + c \frac{\partial y(z, t)}{\partial t} \\ = F_y(z, t), \end{aligned} \tag{6}$$

where EI is the constant bending stiffness, $T(Z)$ is the axial tension of each discrete structural element, m is the mass of each discrete structural element, c is the damping of each discrete structural element, $F_x(z, t)$ and $F_y(z, t)$ are the hydrodynamic forces acting on the surface of each discrete structural element in the inline and crossflow directions, respectively, and $x(z, t)$ and $y(z, t)$ are the displacements of the discrete structural elements as functions of time and position z .

By constructing the element matrix for the structure via the finite element method, the vibration differential equations governing all riser elements are integrated as follows:

$$\mathbf{M}\{\ddot{\mathbf{X}}\} + \mathbf{C}\{\dot{\mathbf{X}}\} + \mathbf{K}\{\mathbf{X}\} = \{\mathbf{F}_{\text{HX}}\}, \tag{7}$$

$$\mathbf{M}\{\ddot{\mathbf{Y}}\} + \mathbf{C}\{\dot{\mathbf{Y}}\} + \mathbf{K}\{\mathbf{Y}\} = \{\mathbf{F}_{\text{HY}}\}, \tag{8}$$

where \mathbf{M} , \mathbf{C} , and \mathbf{K} are the mass, damping, and stiffness matrices, respectively; \mathbf{F}_{HX} and \mathbf{F}_{HY} are the hydrodynamic force vectors in the inline and crossflow directions, respectively; and \mathbf{X} and \mathbf{Y} are the displacement vectors in the inline and crossflow directions, respectively. In addition, the practical damping is replaced by Rayleigh damping to obtain the damping matrices.⁴

C. Thick-strip model

The numerical calculation requires significant resources because of the substantial increase in axial mesh needed to describe the flexible slender riser in 3D. To overcome this problem, the traditional strip model replaces the 3D flow field with several identical 2D flow strips along the riser span, accelerating the numerical calculation while ensuring an accurate simulation.^{4,37} By neglecting the axial correlation of the flow field, this model cannot accurately describe the hydrodynamic forces acting on the complex cross section, nor can it handle the numerical calculation of the periodically varying axial cross section. Therefore, we propose to use the generalized thick-strip model validated by Bao *et al.*,³⁸ which extends the 2D fluid strips to 3D fluid strips. Figure 1 shows a schematic diagram of this model. By introducing the generalized thick-strip model, viv3D-FOAM-SJTU simulates VIV for a flexible riser exposed to uniform flow, capturing the 3D effects of the flow.

The software viv3D-FOAM-SJTU uses the PIMPLE algorithm for the iterative calculation of velocity field and pressure field for all thick strips, and the hydrodynamic forces exerted on discrete structural elements outside the thick strips are obtained by cubic spline interpolation. The governing equations for all riser elements are solved by using the Newmark-beta algorithm³⁹ to acquire the displacements in the inline and crossflow directions of VIV. Moreover, the fluid field and structural vibrations in VIV of a slender flexible riser are coupled by two-way coupling technology.

III. NUMERICAL SETUP

In this paper, all configurations are modified by the same bare flexible riser, following the experiment of Lehn,⁴⁰ and the structural modifications are based on the simulations of Ma *et al.* and Law and Jaiman and the experiments of Huang and Park *et al.*^{28,29,31,41} Figure 2 shows the details of the 3D geometric model and the 2D cross section of the structural elements embodied by each thick fluid strip. The strip length is 0.2D, the groove width is 0.2D, and the groove depth is 0.12D, which remain constant in all configurations. In the configuration of Fig. 2(a), two symmetrical spanwise strips are attached to the

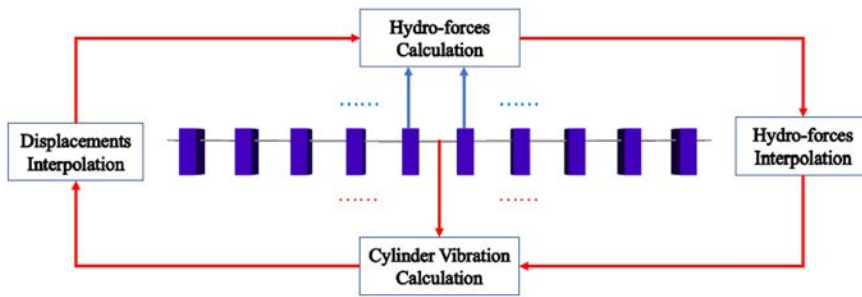


FIG. 1. Schematic diagram of the generalized thick-strip model.

riser surface. The cases of $\alpha = 30^\circ, 45^\circ, 60^\circ, 120^\circ, 135^\circ,$ and 150° with the fixed $t_s = 0.08D$ are first studied to seek an angle for which VIV is suppressed. Various structural arrangements have been designed to further optimize VIV suppression. The configuration of Fig. 2 (case 8) is designed as four symmetrical spanwise strips installed at the riser surface, and the configuration of Fig. 2 (case 9) is the staggered structure of four symmetrical strips. Based on configurations of Fig. 2 (cases 2, 8, and 9) by introducing the two symmetrical spanwise grooves located at 90° with respect to the stagnation point at the front of the riser cross section, we obtain the configurations shown in Fig. 2 (cases 10, 11, and 12). Moreover, apart from the configuration of Fig. 2 (case 2), all other configurations are simulated with two different thicknesses $t_s = 0.05D$ and $0.08D$, which are suitable for suppressing the VIV of the riser.⁴² Risers for all configurations are subjected to a uniform current of 0.2 m/s , and Table I shows all the cases studied herein. The numerical results for cases 2 and 7 are from Hu *et al.*⁴² To facilitate the comparison and analysis of the numerical results, all configurations share a set of main structural parameters, which are consistent with the bare flexible riser (see Table II).

Figure 3(a) shows that the numerical calculation domain for all cases covers 10 uniform thick fluid strips in the vertical direction of

the riser. Considering the flow direction and the requirement to capture the 3D nature of the flow field, a cuboid of size $20D \times 40D \times (1/100)L$ is selected as the thick-strip domain. The center of gravity of the riser is $10D$ from the inlet boundary and $10D$ from the left boundary. To ensure accurate numerical calculations of pressure and velocity in the viscous sublayer on the riser surface [as marked in Figs. 3(d)–3(g)], the meshes in the boundary layer are refined so that y^+ is less than 3.0 in all cases. The boundary conditions common to each thick-strip in Fig. 3(b) are as follows: The inlet boundary is assigned the velocity inlet condition; the outlet boundary is assigned the pressure outlet condition; the top, bottom, left, and right boundaries are assigned the symmetry conditions; the surface of each structural element is assigned the no-slip boundary condition; and the two ends of the flexible slender riser are assigned simple boundary conditions. The grid is updated by using the dynamic “displacement Laplacian” grid technique when the riser vibrates in the inline and crossflow directions. The total number of discrete structural elements for all riser configurations is fixed at 200 for all cases. To ensure stable convergence for all simulations, we use a suitable time step to guarantee a Courant number (C_o) less than 5.0. The definition of the Courant number is as follows:

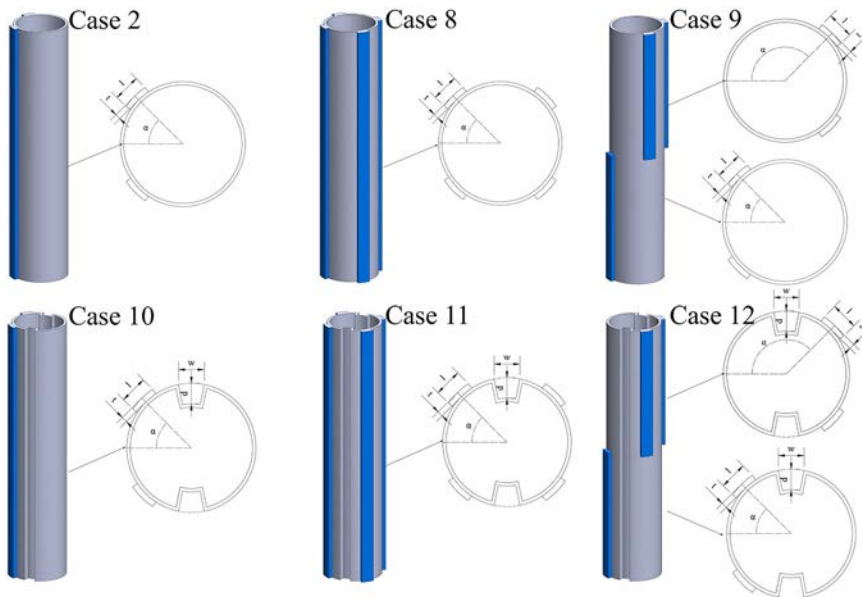


FIG. 2. Schematic diagram of 3D geometric model and 2D cross section of structural elements contained in each thick fluid strip.

TABLE I. Cases for different configurations.

Configuration	Strip thickness (t_s)	Strip angle (α)	Groove angle (α_0)
Case 1	a	0.08D	30°
Case 2	a	0.08D	45°
Case 3	a	0.08D	60°
Case 4	a	0.08D	120°
Case 5	a	0.08D	135°
Case 6	a	0.08D	150°
Case 7	a	0.05D	45°
Case 8	b	0.08D	45°/135°
Case 9	c	0.08D	45°/135°
Case 10	d	0.08D	45°
Case 11	e	0.08D	45°/135°
Case 12	f	0.08D	45°/135°
Case 13	b	0.05D	45°/135°
Case 14	c	0.05D	45°/135°
Case 15	d	0.05D	45°
Case 16	e	0.05D	45°/135°
Case 17	f	0.05D	45°/135°

$$C_o = \frac{\delta t |\mathbf{U}|}{\delta x}, \tag{9}$$

where δt is the time step, $|\mathbf{U}|$ is the module of velocity vector in a grid cell, and δx is the grid length in the velocity direction.

IV. VALIDATION AND VERIFICATION

The root mean square (RMS) displacements along the riser span and frequency responses for crossflow and inline displacements are used to validate the accuracy of the numerical calculation solved by implementing the SST-DDES model in viv3D-FOAM-SJTU and

TABLE II. Main riser parameters for all configurations.

Property	Value	Units
Length	L	9.63 m
Diameter	D	20 mm
Structural stiffness	EI	135.4 Nm^2
Top tension	T	817 N
Mass ratio	m^*	2.23
Aspect ratio	L/D	481.5
Flow velocity	U	0.2 m/s
First natural frequency	f_{n1}	1.79 Hz
Second natural frequency	f_{n2}	3.67 Hz

verifying the convergence herein. The equations for the RMS displacements are

$$A_{y,RMS}(z) = \sqrt{\sum_{t=t_s}^{t_e} [A_y(z, t)]^2}, \tag{10}$$

$$A_{x,RMS}(z) = \sqrt{\sum_{t=t_s}^{t_e} [A_x(z, t) - \bar{A}_x(z)]^2}, \tag{11}$$

where $A_{y,RMS}$ is the RMS crossflow displacement along the riser span, $A_{x,RMS}$ is the RMS inline displacement along the riser span, z is the axial location, t_s is the beginning of computation, t_e is the end of computation, and $\bar{A}_x(z)$ is the inline equilibrium position for the entire computation.

We use a fast Fourier transform to transform the time-domain signal into the frequency domain to obtain the corresponding power spectral density (PSD), so as to study the vibration characteristics of the frequency domain. The equation for the fast Fourier transform is

$$H(f) = \int_{-\infty}^{\infty} h(t)e^{-ift} dt, \tag{12}$$

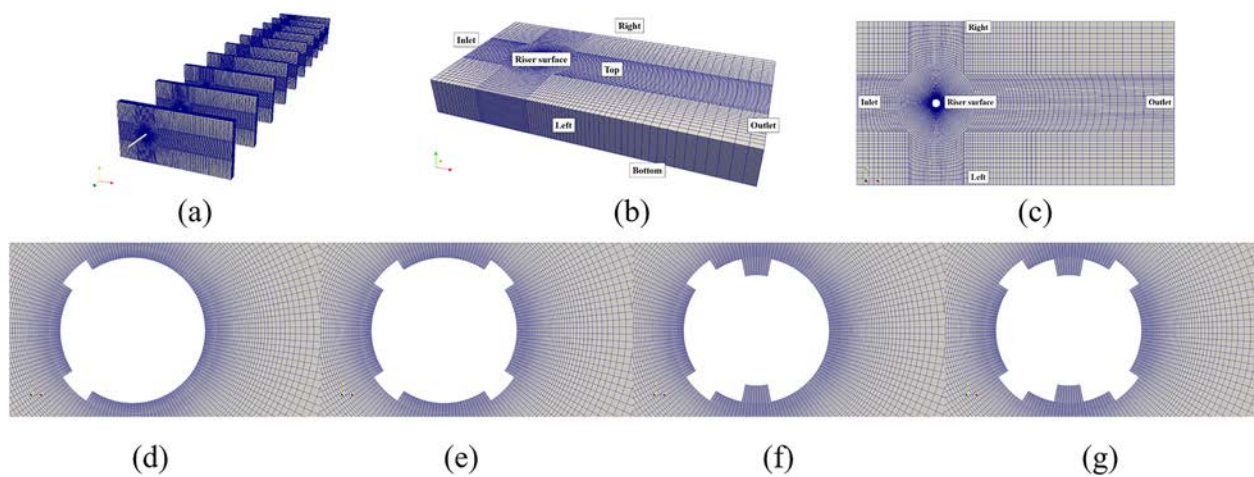


FIG. 3. Computational grid and boundary conditions. (a) Computational model, (b) computational domain of a fluid strip, (c) vertical view of a fluid strip (d) grid near the riser (case 2), (e) grid near the riser (case 8), (f) grid near the riser (case 10), (g) grid near the riser (case 11).

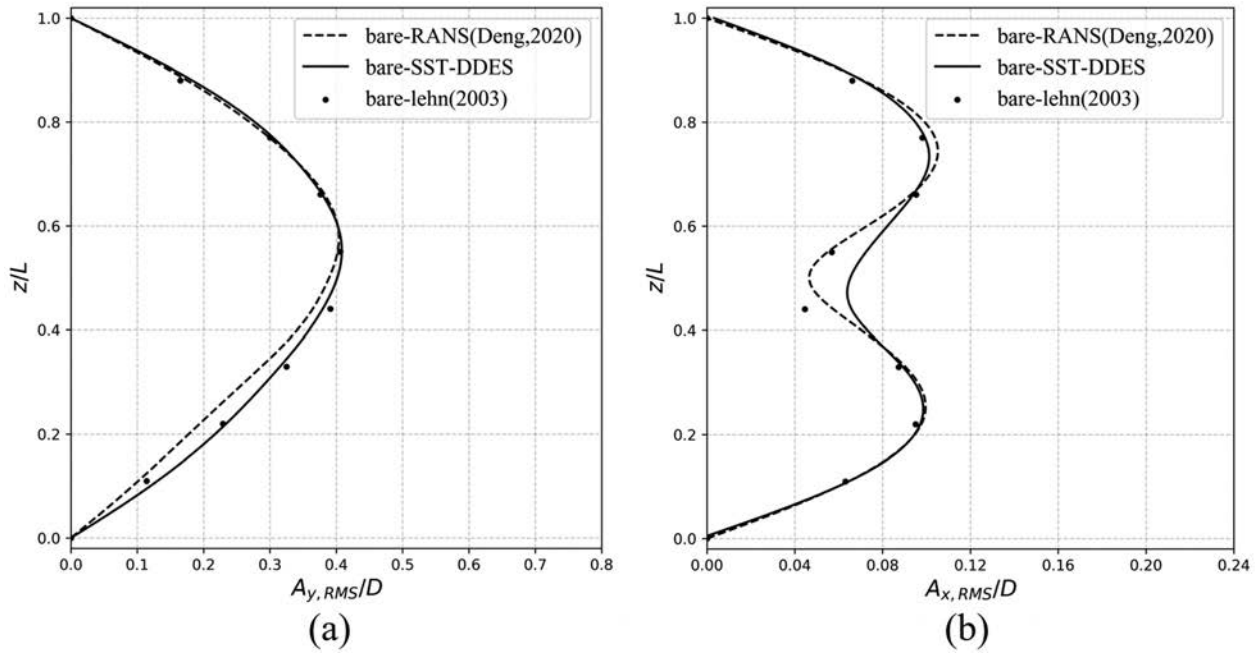


FIG. 4. Dimensionless RMS displacement along riser span. (a) Crossflow, (b) inline.

where $h(t)$ is the time-domain signal, $H(f)$ is the spectrum of $h(t)$, and f is the frequency.

Figures 4(a) and 4(b) compare the numerical results for the dimensionless crossflow and inline RMS displacements, respectively, along the span of the bare riser. These are obtained by using the RANS model³³ and the SST-DDES model, both carried implemented in viv3D-FOAM-SJTU with the same grid (3.07 million elements). The results are also compared with the experimental results of Lehn.⁴⁰ As shown in Fig. 4(a), the SST-DDES model, like the RANS model, captures the maximum dimensionless RMS crossflow displacement of around 0.407D at 0.55L. In addition, the dimensionless RMS crossflow displacements given by the SST-DDES model at 0.11L, 0.22L, 0.33L, and 0.44L are closer to the experimental data

than that given by the RANS model. Figure 4(b) shows that the dimensionless RMS inline displacements at 0.11L, 0.22L, 0.33L, 0.66L, 0.77L, and 0.88L predicted by the SST-DDES model are consistent with the numerical values predicted by the RANS method and with the experimental data, whereas a discrepancy still exists between the values predicted at 0.44L and 0.55L and the experimental data.

The frequency response is compared and analyzed below. It can be seen from Fig. 5(a) that the highest peak frequency for the crossflow displacement at 0.2L in the experiment is 1.57 Hz, corresponding to the first-order vibration mode form of the riser, and there are some weak high-order frequency components. The highest peak frequency for inline displacement at 0.2L is 3.26 Hz, corresponding to the

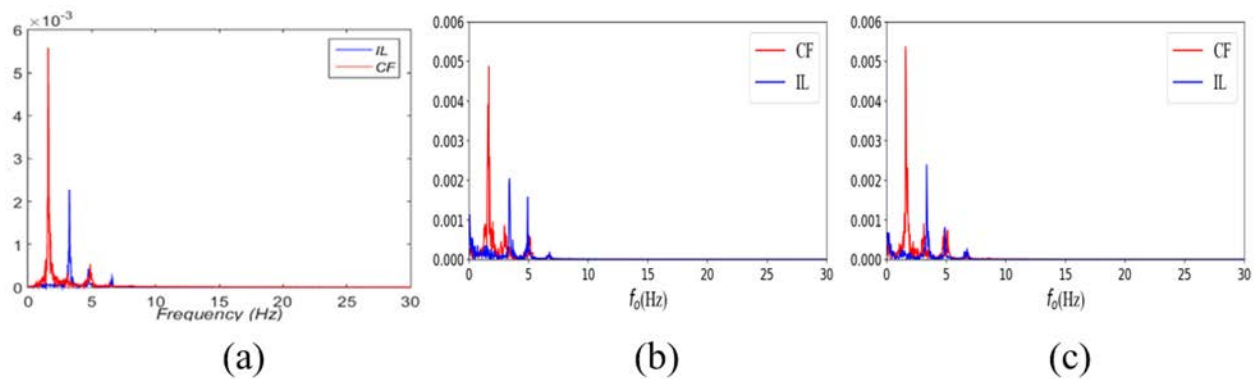


FIG. 5. PSDs of crossflow (CF) and inline (IL) displacements at 0.2L. (a) Experimental results of Lehn,⁴⁰ (b) numerical results of RANS model,³³ (c) numerical results of SST-DDES model.

second-order vibration mode form of the riser, and there are also some weak high-order frequency components. In the numerical simulation, the highest peak frequencies for the crossflow displacement at 0.2L captured by the RANS model and the SST-DDES model are 1.66 and 1.60 Hz, respectively, showing that the results of the SST-DDES model are closer to the experimental results. Similar to the experimental results, both the RANS model and the SST-DDES model capture weak high-order frequency components. The highest peak frequencies for the inline displacement at 0.2L captured by the RANS model and the SST-DDES model are 3.36 and 3.39 Hz, respectively, revealing that the numerical results are very close and larger than the experimental results. At the same time, in terms of capturing higher-order frequency components, the results obtained by the SST-DDES model are closer to the experimental results in the inline direction. The above analysis testifies to the accuracy of the SST-DDES model for predicting the VIV of the flexible riser.

Case 8 with three sets of grids (cases 8–1, 8–2, and 8–3 in Table III) is adopted as the benchmark to verify grid independence. Figure 6(a) shows that the dimensionless RMS displacements with different grids have the same first-order mode form in the crossflow direction, and the locations of maximum nondimensional RMS crossflow remain almost stationary, both near 0.49L. Meanwhile, the maximum nondimensional RMS crossflow displacements for the three sets of grids are 0.110D, 0.116D, and 0.115D, and the numerical error is less than 5%.

Figure 6(b) shows that the mode form of the nondimensional RMS displacements for coarse, medium, and fine grids are roughly the same in the inline direction. The maximum nondimensional RMS inline displacements occur at slightly different locations: 0.51L, 0.48L, and 0.50L, respectively. The three sets of grids also produce numerical errors in the prediction of the maximum nondimensional RMS inline displacements (0.0256D, 0.0262D, and 0.0280D, respectively), and the maximum numerical error is about 8%. Therefore, the average numerical prediction error is acceptable for the nondimensional RMS displacement extremum and the corresponding axial position computed in the three computational grids.

Case 8 with three sets of timesteps (cases 8–3, 8–4, and 8–5 in Table III) is adopted to verify time step independence. As shown in Fig. 6(c), the maximum dimensionless RMS crossflow displacements for cases 8–4 and 8–5 are 0.110D and 0.112D, and the numerical error is less than 5% compared to that of case 8–3. Meanwhile, different sets of timesteps also produce numerical errors in the prediction of the maximum dimensionless RMS inline displacements (0.0276D and 0.0265D for cases 8–4 and 8–5) in Fig. 6(d), and the maximum numerical error is about 5% compared to that of case 8–3.

The frequency response is compared and analyzed below. As shown in Fig. 7, the highest peak frequencies for the crossflow displacement at 0.2L captured by grids I, II, and III are 2.53, 2.49, and 2.46 Hz, respectively, and the numerical error is less than 3%. The frequencies for the inline displacement at 0.2L both exist no obvious peak. Therefore, there are some errors in the frequency prediction of the three sets of grids, and the average error is within the acceptable range. Meanwhile, the highest peak frequencies for the crossflow displacement at 0.2L captured in cases 8–4 and 8–5 are 2.48 and 2.45 Hz, and the numerical error is less than 1% compared to that of case 8–3, indicating that the effect of different sets of timesteps on frequency response is limited.

Considering the requirement of accurately capturing the wake field of the complex cross sections and the efficiency of numerical calculation at different configurations, the fine grid with time step of 0.001 s serves herein as the reference. Subsequent configurations adjust the grid divisions according to the difference in position and thickness of the strips and the presence or absence of grooves, but the grid topology remains the same.

V. CYLINDRICAL RISER WITH TWO SYMMETRICAL SPANWISE STRIPS

This section details the investigation of how the installation angle between two symmetrical spanwise strips affects the VIV of the riser and explores the mechanism by which VIV of the flexible riser is suppressed or enhanced.

Figure 8 compares the dimensionless RMS crossflow displacements with the RMS inline displacements along the span of the bare riser and for a riser with two spanwise symmetrical strips with $\alpha = 30^\circ, 45^\circ, 60^\circ, 120^\circ, 135^\circ, \text{ and } 150^\circ$. Table IV lists the maximum dimensionless RMS displacements and the corresponding axial positions. Figure 8(a) shows that, for all cases displayed, the dimensionless RMS crossflow displacements are due to first-order vibrations at similar axial positions with the maximum amplitude close to 0.5L. Unlike the bare riser, the maximum dimensionless RMS crossflow displacement drops to 0.297D (a drop of 40.7% with respect to the bare riser) for case 1. As α approaches 45° , the maximum dimensionless RMS crossflow displacement drops further to 0.139D for case 2 (a drop of 65.8% with respect to the bare riser). However, compared with the bare riser, case 3 with $\alpha = 60^\circ$ increases the dimensionless RMS crossflow displacement, and its maximum increases 49.4% with respect to the bare riser to 0.608D. When two symmetrical strips are installed at the trailing edge of the riser, the dimensionless RMS crossflow displacement of cases 4–6 are both suppressed, and their maxima are 0.343D, 0.162D, and 0.142D (decrements of 15.8%, 60.2%, and 65.1%, respectively, with respect to the bare riser). In summary, except for

TABLE III. Details of convergence study.

	Grid	Grid quantity	y+	Max aspect ratio	time step (s)
Case 8-1	Grid I (Coarse)	3.24×10^6	2.73	55	0.001
Case 8-2	Grid II (Middle)	4.42×10^6	2.73	47	0.001
Case 8-3	Grid III (Fine)	5.52×10^6	2.73	41	0.001
Case 8-4	Grid III (Fine)	5.52×10^6	2.73	41	0.0012
Case 8-5	Grid III (Fine)	5.52×10^6	2.73	41	0.0005

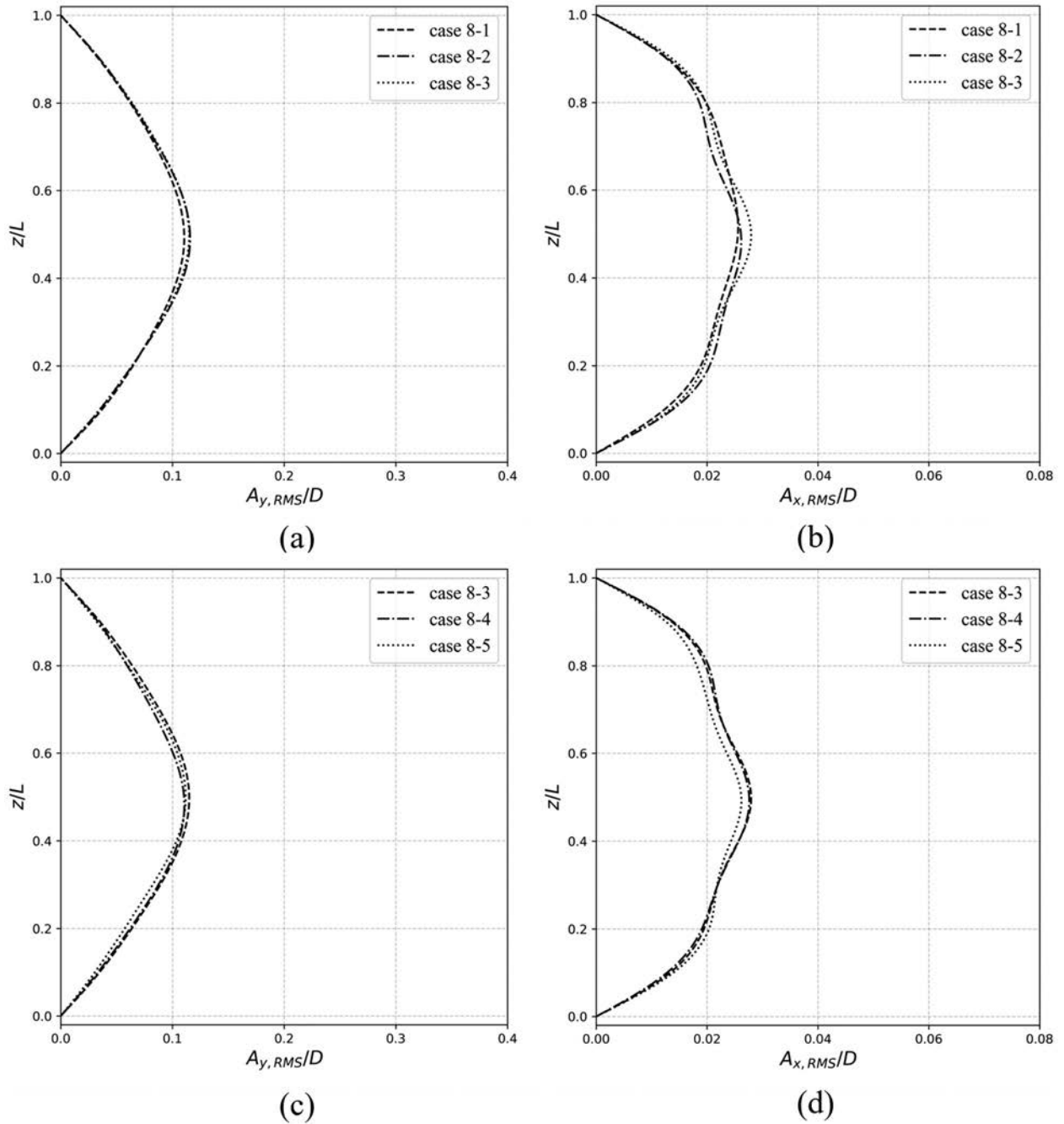


FIG. 6. Dimensionless RMS displacement along riser span. (a) Crossflow for three sets of grids, (b) inline for three sets of grids, (c) crossflow for three sets of timesteps, (d) inline for three sets of timesteps.

case 3 with $\alpha = 60^\circ$, the other cases suppress to some extent the dimensionless RMS crossflow displacement. The cases with $\alpha = 45^\circ, 135^\circ$, and 150° thus suppress VIV better than the other cases.

Figure 8(b) shows that the installation angle of the symmetrical strips on the riser surface exerts a more complex effect on the dimensionless RMS displacement in the inline direction than in the crossflow

direction. The vibration form of the dimensionless RMS inline displacement changes: case 1 produces the third-order vibration form, cases 2, 5, and 6 produce the second-order vibration form, and cases 3 and 4 produce the first-order vibration form. Therefore, the maxima of the dimensionless RMS inline displacements in the axial direction differ for all cases displayed. Moreover, the maximum of the

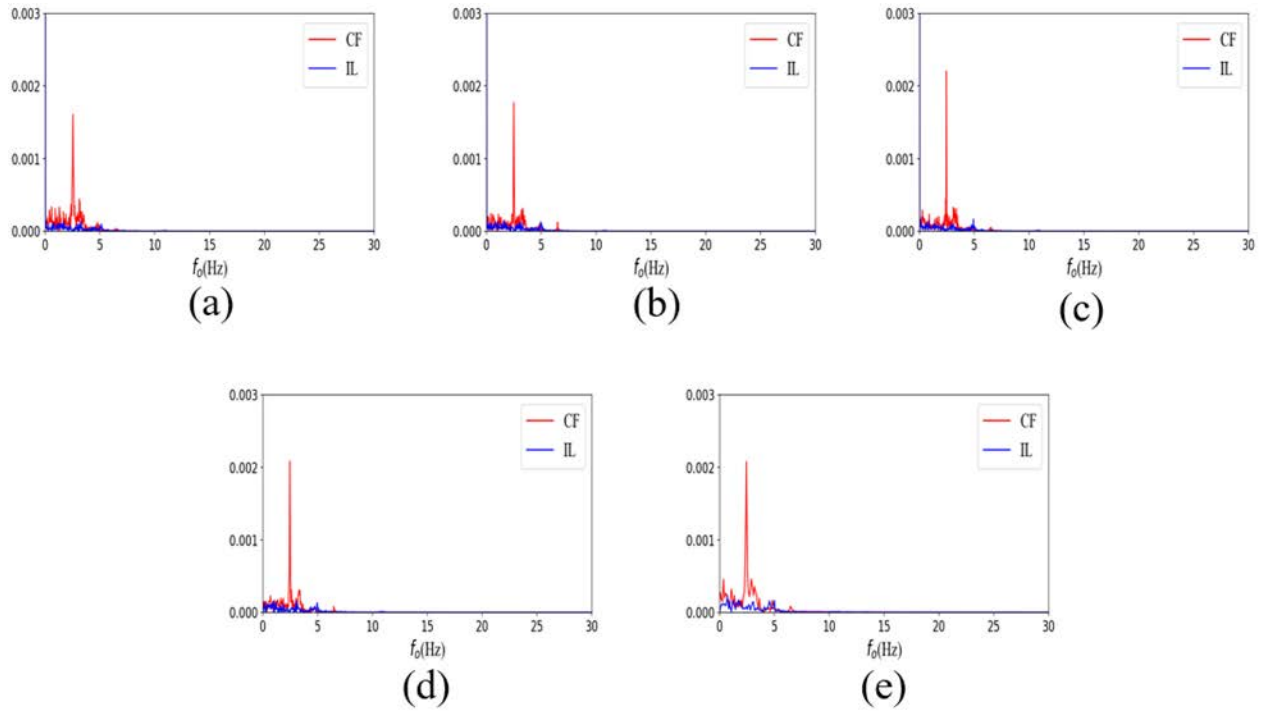


FIG. 7. PSDs of crossflow (CF) and inline (IL) displacements at 0.2L. (a) Case 8-1, (b) case 8-2, (c) case 8-3, (d) case 8-4, (e) case 8-5.

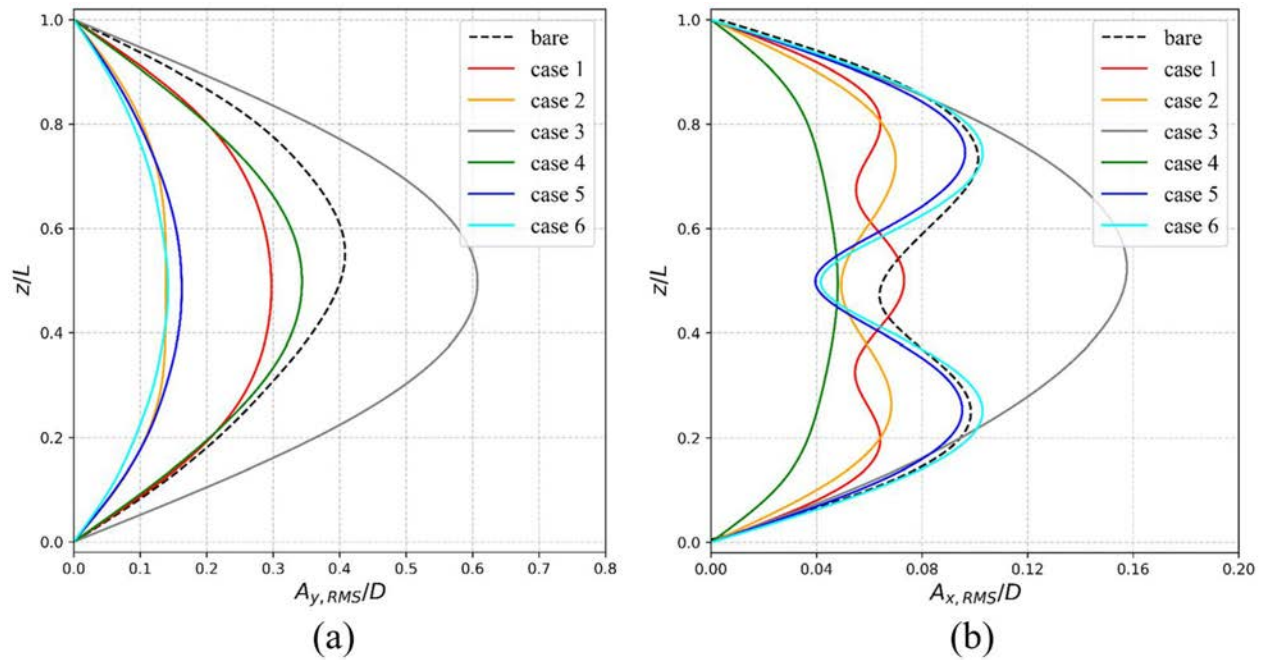


FIG. 8. Dimensionless RMS displacement along riser span. (a) Crossflow, (b) inline.

TABLE IV. Maximum dimensionless RMS displacements and corresponding axial locations.

	Crossflow		Inline	
	$A_y, RMS_{max}/D$	z/L	$A_x, RMS_{max}/D$	z/L
Bare riser	0.407	0.550	0.101	0.740
Case 1	0.297	0.485	0.073	0.500
Case 2 ⁴²	0.139	0.510	0.070	0.730
Case 3	0.608	0.500	0.158	0.525
Case 4	0.343	0.500	0.048	0.495
Case 5	0.162	0.485	0.096	0.745
Case 6	0.142	0.485	0.103	0.250

dimensionless RMS inline displacement for case 3 (0.158D) significantly exceeds that of the bare riser, whereas the maximum of the dimensionless RMS inline displacement of cases 5 (0.096D) and 6 (0.103D) are close to that of the bare riser. With respect to the bare riser, the maximum dimensionless RMS inline displacements for cases 1, 2, and 4 drop 27.7%, 30.7%, and 52.5% to 0.073D, 0.070D, and 0.048D, respectively. In conclusion, for all cases of Fig. 8, the overall decrease in the dimensionless RMS displacement in the inline direction is less than that in the crossflow direction.

To further analyze the VIV of the flexible riser, we introduce the modal decomposition method to transform the time-history vibration displacements into a sum of vibration mode weights in the crossflow and inline directions. The relevant equations are as follows:

$$\varphi_n(z) = \sin\left(\frac{n\pi}{L}z\right), \tag{13}$$

$$A_y(z, t) = \sum_{n=1}^N w_{yn}(t)\varphi_n(z), \tag{14}$$

$$A_x(z, t) = \sum_{n=1}^N w_{xn}(t)\varphi_n(z), \tag{15}$$

where $n = 1, 2, 3, \dots$ is the mode number, $A_y(z, t)$ is the vibration displacement of the flexible riser in the crossflow direction, $A_x(z, t)$ is the vibration displacement of the flexible riser in the inline direction, $w_{yn}(t)$ is the modal weight of mode n in the crossflow direction, $w_{xn}(t)$ is the modal weight of mode n in the inline direction, $\varphi_n(z)$ is the modal shape for mode n , and N is the maximum mode number.

Figure 9 shows crossflow vibration mode weights as functions of time and the corresponding PSDs of the bare riser and of cases 1–6. The red lines locate the highest peaks, and the corresponding frequency is given in the legend. For the bare riser and cases 1–6, the dominant crossflow vibration modes are fixed at the first-order vibration mode for the time range considered, although the vibration amplitudes of the second-order mode are visible for the bare riser and for cases 1–3. The vibration amplitude of the first-order crossflow mode for case 1 is less than that for the bare riser, which is nearly constant over the given time range, whereas the corresponding frequency (2.196 Hz) is greater than that of the bare riser, and a similar situation occurs for case 4. For the first-order crossflow mode, the main difference between cases 2 and 1 is that the vibration amplitude goes from

nearly constant to wave-like, and the vibration amplitude of case 2 is further reduced during the time range displayed. Cases 1, 2, and 4 all suppress the vibration amplitude of the first-order crossflow mode by increasing the corresponding frequency to differ from the first-order natural frequency. The installation angle $\alpha = 60^\circ$ for the two symmetrical strips on the riser surface, so the corresponding first-order crossflow mode vibration frequency for case 3 (1.131 Hz) is relatively low, and the vibration amplitudes are much greater than that of the bare riser for the other cases displayed, which results are similar with the galloping mentioned by Ma *et al.*³¹ Compared with the bare riser, the vibration amplitudes of the first-order crossflow mode for cases 5 and 6 are suppressed by the decrease in the corresponding vibration frequencies (1.364 and 1.464 Hz), and the vibration amplitudes at both frequencies undergo wave-like oscillations over the time range displayed.

Figure 10 shows the inline vibration mode weights as functions of time and the corresponding PSDs of the bare riser and of cases 1–6. The vibration amplitude of the second-order inline mode for cases 1–6 is both weaker than that of the bare riser. In case 1, the corresponding vibration frequency has two amplitude peaks, one of high frequency and one of low frequency, implying that some low-frequency vibrations contribute to the second-order inline vibration mode. The vibration amplitudes of the third-order inline mode exceed the amplitudes of the inline vibration modes of other orders, making the third-order mode the dominant inline vibration mode. Like the bare riser, the vibration amplitudes of the second-order inline modes of cases 2, 5, and 6 exceed the amplitudes of inline vibration modes of other orders, and only one peak exists at the corresponding vibration frequency. Compared with the other cases in Fig. 10, case 3 produces the largest-amplitude first-order inline vibration modes, which is more in line with the galloping-vibration phenomenon. The vibration amplitudes of the first-order inline mode of case 4 are greater than those of the inline vibration modes of other orders. However, compared with the other cases in Fig. 10, no clear difference appears in the vibration amplitudes of first-order inline modes over the given time range.

In order to analyze the vortex shedding characteristics of 3D wake field, Q criterion is used to visualize the flow field. The equation for the Q is

$$Q = -\frac{1}{2} \left[\left(\frac{\partial v_x}{\partial x} \right)^2 + \left(\frac{\partial v_y}{\partial y} \right)^2 + \left(\frac{\partial v_z}{\partial z} \right)^2 \right] - \frac{\partial v_x}{\partial y} \frac{\partial v_y}{\partial x} - \frac{\partial v_x}{\partial z} \frac{\partial v_z}{\partial x} - \frac{\partial v_y}{\partial z} \frac{\partial v_z}{\partial y}, \tag{16}$$

where v_x , v_y , and v_z are the velocities in x, y, and z directions.

Figures 11 and 12 show the instantaneous 3D vortex structures the instantaneous 2D vortex shedding of the bare riser and of cases 1–6. The flow field for bare riser reveals the complexity of the 3D vortex structures due to the thick fluid strips, which include cylindrical-, wavy-, and smaller discrete-type vortices. Moreover, the vortex structures at different positions in the fluid strips also differ; for example, the cylindrical vortex structure dominates in the seventh fluid strips, whereas wavy and smaller discrete vortex structures dominate in the third and fifth fluid strips. Two symmetrical spanwise strips are fixed to the leading edge of the riser surface at installation angles $\alpha = 30^\circ$, 45° , and 60° [cases 1, 2, and 3], and the magnitude of the cylindrical vortex structures increases at the position of each fluid strip, which

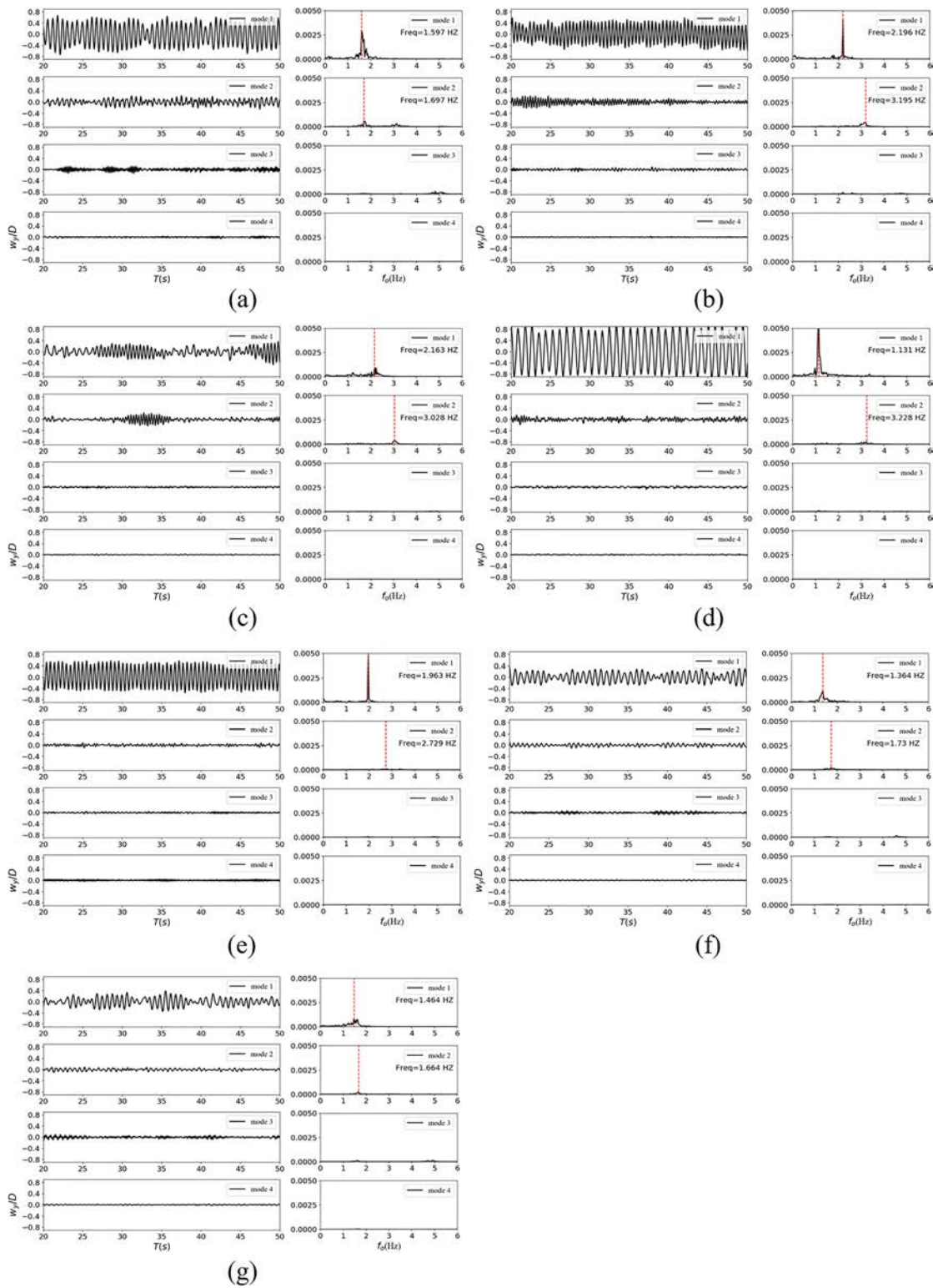


FIG. 9. Crossflow vibration mode weights (w_i/D) as functions of time and the corresponding PSDs. (a) bare riser, (b) case 1, (c) case 2, (d) case 3, (e) case 4, (f) case 5, (g) case 6.

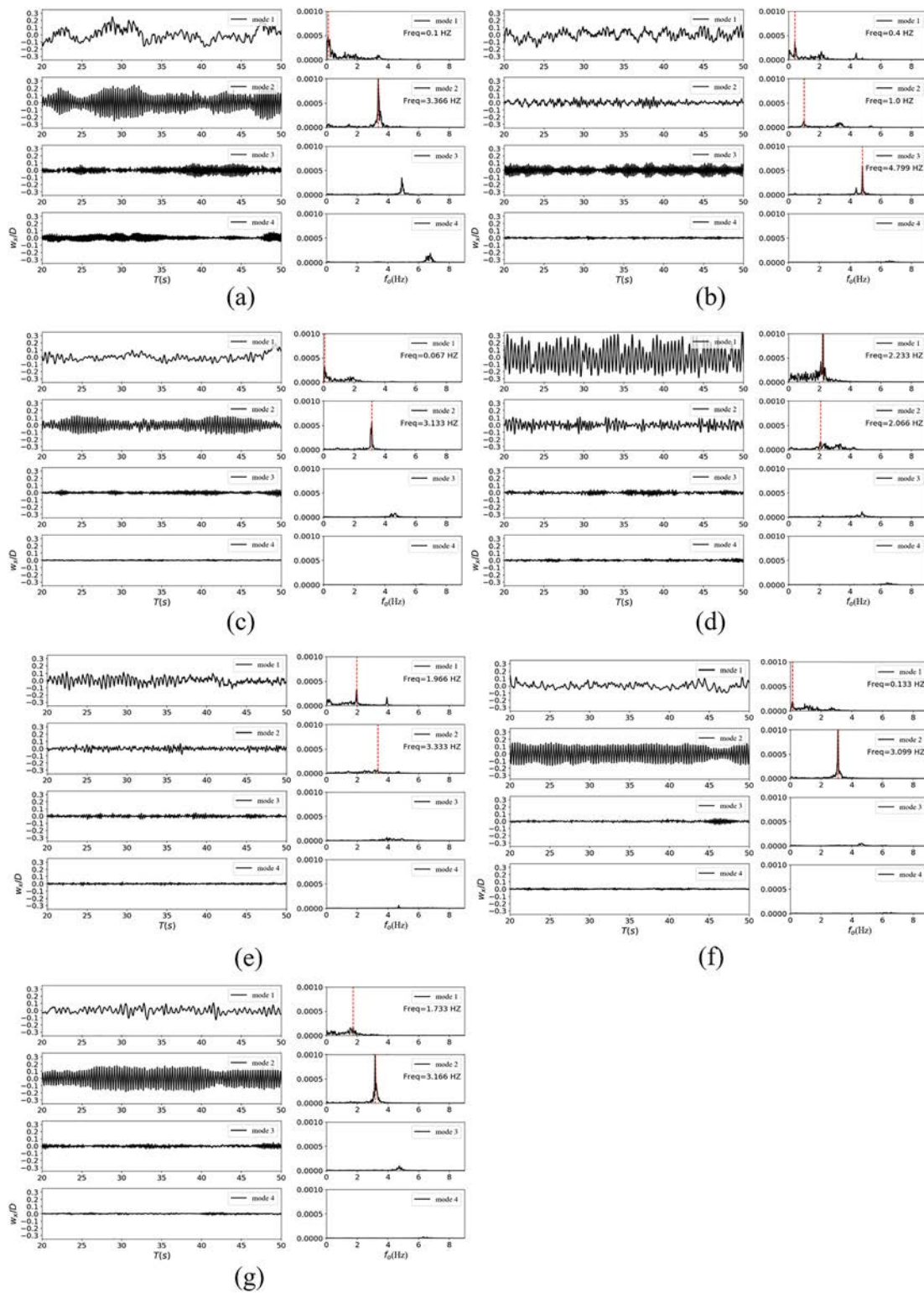
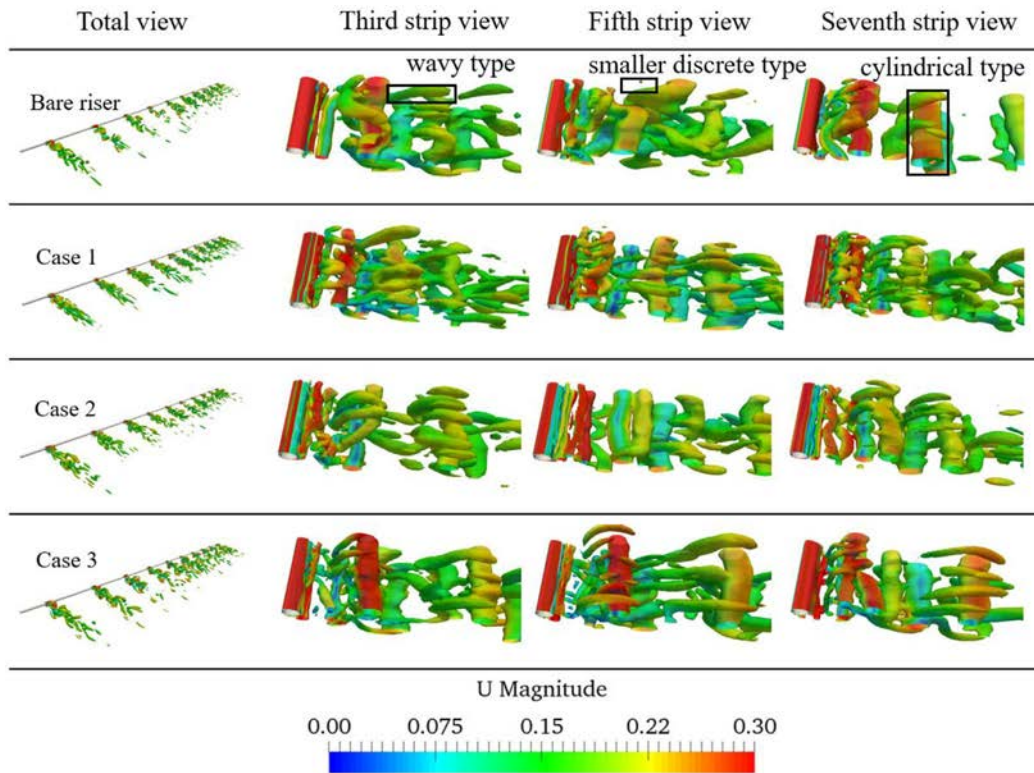
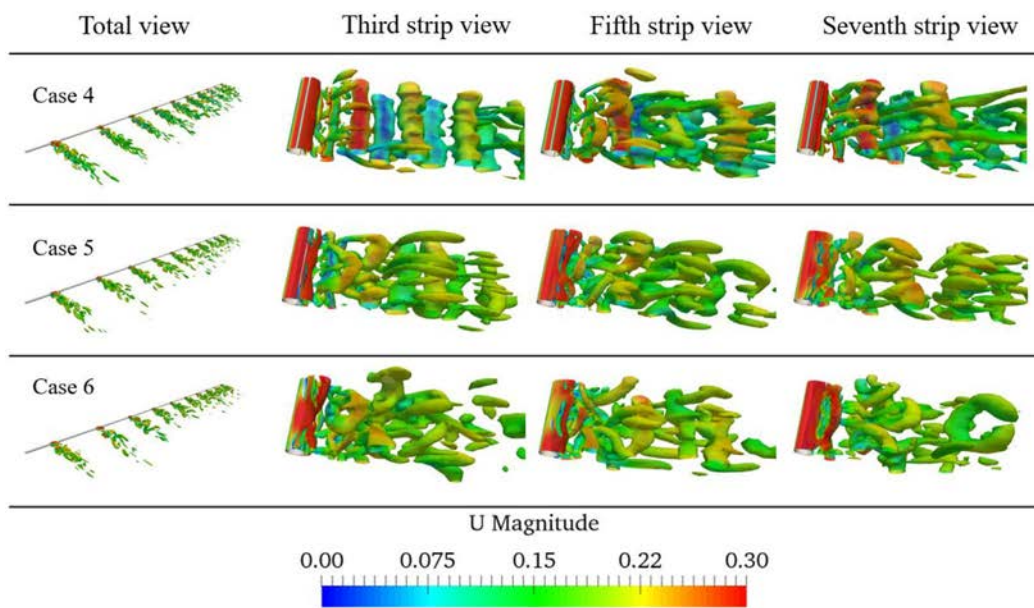


FIG. 10. Inline vibration mode weights (w_i/D) as functions of time and the corresponding PSDs. (a) bare riser, (b) case 1, (c) case 2, (d) case 3, (e) case 4, (f) case 5, (g) case 6.



(a)



(b)

FIG. 11. Instantaneous vortex structures through the Q criterion ($Q = 5$) of three fluid strips for (a) bare riser and cases 1–3, (b) cases 4–6 at 47 s; from left to right: Total, third strip, fifth strip, and seventh strip.

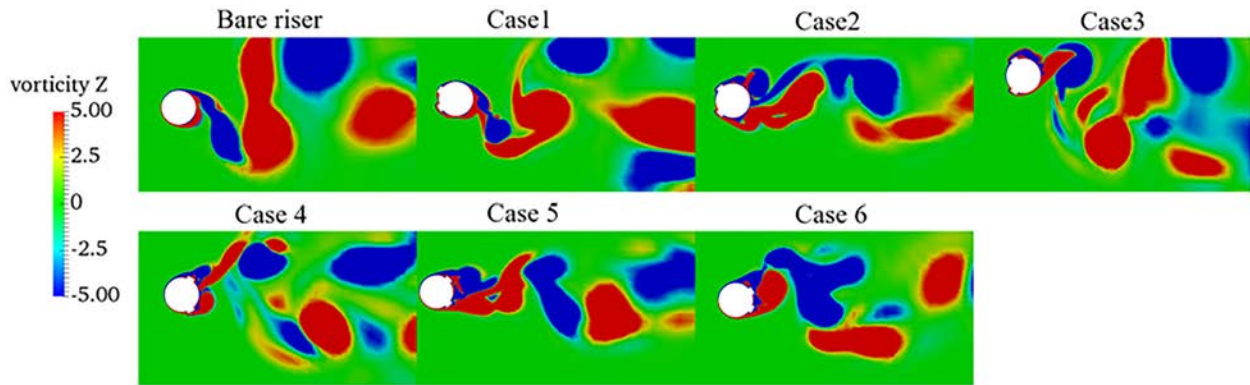


FIG. 12. Instantaneous z vorticity ($\omega_z = dv_y/dx - dv_x/dy$) at the same axial location $z = 5.3$ m for bare riser, and cases 1–6 at 46 s.

reflects an improved 3D vortex shedding consistency, and an increase in crossflow vibration frequency of cases 1 and 2. When two spanwise symmetrical strips are mounted near the trailing edge of the riser surface, the number of wavy- and smaller discrete-type vortex structures gradually increases with increasing α until they become dominant in all fluid strips displayed for case 6. This result implies that this arrangement confines the generation of cylindrical-type vortex structures and destroys the stability of the periodic variation of the wake region, which can bring a decrease in crossflow vibration frequency.

As shown in Fig. 12, unlike the vortex shedding of the bare riser, forced flow separation occurs at the two symmetrical strips, which alters the 2D vortex shedding. Compared with the 2D vortex shedding of the bare riser, case 3 shows that the width of the vortex street and the number of vortices both increase, thereby increasing the fluid forces and enhancing the vibrations. However, the reduced width of the vortex street and the number of vortices for cases 2, 5, and 6 appear clearly in comparison with the bare riser, which weakens the vibrations. These results illustrate that suppressing VIV requires selecting an installation angle α that is consistent with the results given in Fig. 8.

This section investigates the correlation of the fluctuating lift forces along the spanwise direction at the fifth fluid strip, which may be expressed as

$$R = \frac{\sum (E_l - \bar{E}_l)(E'_l - \bar{E}'_l)}{\sqrt{\sum (E_l^2 - \bar{E}_l^2)(E'^2_l - \bar{E}'^2_l)}}, \quad (17)$$

where E_l is the lift coefficient of the bottom section of the structural elements at the fifth fluid strip, and E'_l is the lift coefficient of the other sections along the span of structural elements at the fifth fluid strip. \bar{E}_l and \bar{E}'_l are the time-averaged lift coefficients.

Figure 13 shows the lift correlation coefficient R as a function of z along the span of structural elements at the fifth fluid strip for the bare riser and for cases 1–6. Cases 1–3 show similar relative drops in the correlation coefficients, which are all smaller than that of the bare riser, indicating that the lift is more consistent along the spanwise direction at the fifth fluid strip. This is consistent with the conclusion that the consistency of the 3D vortex structure of the three cases is improved compared to bare riser in Fig. 11. The reduced relative correlation coefficients for cases 4–6 are close to or slightly greater than that for

the bare riser, which means the change in lift in the spanwise direction is slightly greater for cases 4–6 than for cases 1–3.

This section investigates the distribution of skin friction around the center cross section of the structural elements at the fifth fluid strip. The skin friction τ is expressed as

$$\tau = \frac{\tau_0}{\rho U^2} \sqrt{Re}, \quad (18)$$

where τ_0 is the surface shear stress of the structural elements at the fifth fluid strip. $\tau = 0$ means that the boundary layer is separated and the velocity gradient on the structure surface vanishes.

Figure 14 shows the skin friction as a function of the peripheral angle of the cross section for the bare riser and for cases 1–6. The flow separation point Φ_s , forced separation point Φ_{fs} , and reattachment point Φ_r are all marked. For cases 1 and 2, the symmetrical strips installed on the leading edge of the riser cause the flow to separate, so the shear stress suddenly increases here before dropping back to its original value at the reattachment point Φ_r . This means that the boundary layer is recreated at the reattachment point to form a secondary flow separation, thereby delaying the boundary layer separation and compressing the width of the vortex street bring VIV inhibition. However, for case 3, the sudden change of the shear stress still occurs at the symmetrical strips; however, due to the large angle α , no stable reattachment point forms, so flow separation occurs prematurely compared with the bare riser. This implies that the vortices are generated in advance and enhance VIVs. As shown in Figs. 14(e)–14(g), because the boundary layer flow separation occurs before the symmetrical

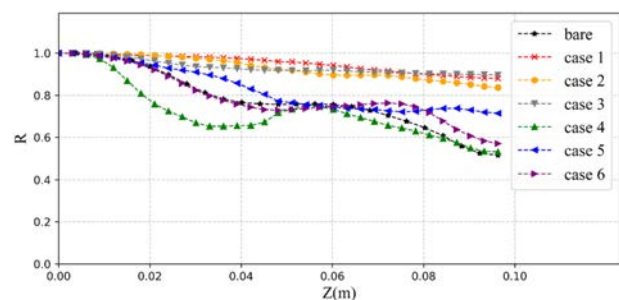


FIG. 13. Correlation coefficient R of the sectional lift at the fifth fluid strip.

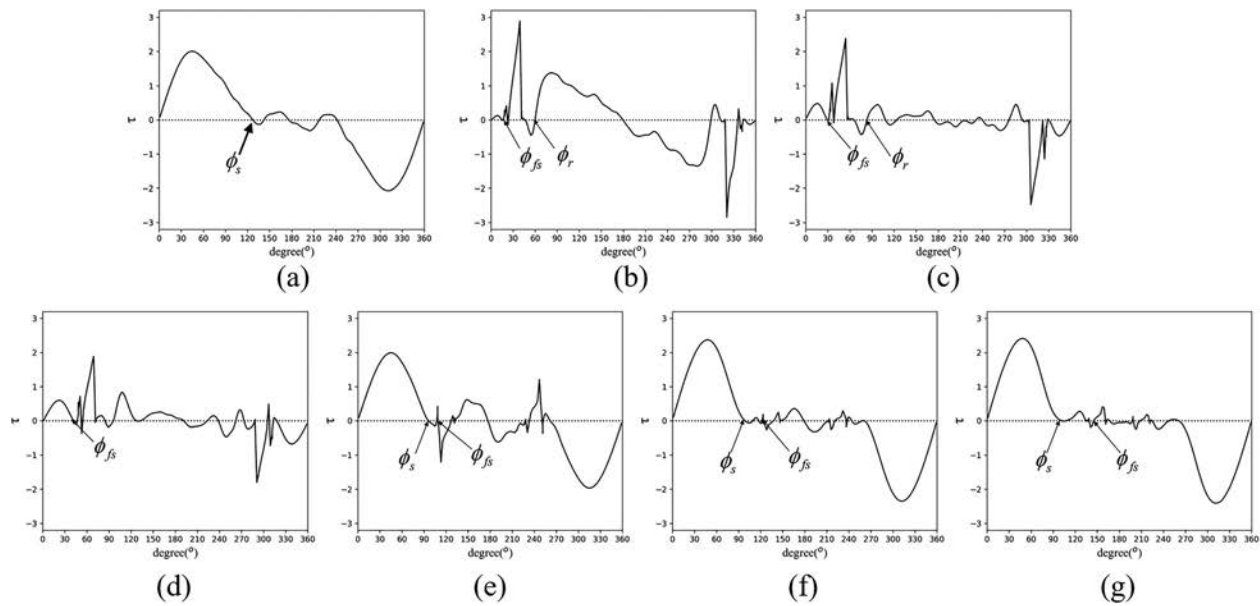


FIG. 14. Skin friction distribution along peripheral angle of cross section at the fifth fluid strip. (a) bare riser, (b) case 1, (c) case 2, (d) case 3, (e) case 4, (f) case 5, (g) case 6.

strips (for cases 4–6), the influence of the symmetrical strips on the boundary layer is weakened, and they instead mainly affect the formation and development of the vortices in the wake region.

This section examines the distribution of local pressure around the center cross section of the structural elements at the fifth fluid strip. The local pressure distribution is quantified by the dimensionless pressure coefficient

$$c_p = \frac{p_s - p_\infty}{0.5\rho U^2}, \quad (19)$$

where p_s is the pressure as a function of the peripheral angle of the cross section, and p_∞ is the static pressure of the current at infinity.

The pressure distribution of the flow over the different cross sections of the bare riser and of cases 1–6 is compared in Fig. 15 at the fifth fluid strip. For case 1, a sharp drop in pressure occurs as the flow encounters the symmetrical strips around 30° , followed by a slight rebound. Similar situations occur in cases 2–4. However, the pressure distributions for cases 5 and 6 are both similar to that of the bare riser, indicating that the symmetrical strips have a limited effect on the pressure distribution for installation angles $\alpha \geq 135^\circ$. Moreover, the differentials between the upstream and downstream pressure coefficients for cases 1–4 are 3.68, 2.72, 2.70, and 3.42, respectively, which are greater than that of the bare riser (2.52). At $Re = 4000$, most of the total drag comes from the differential pressure drag, so the above cases reflect an enhancement of the total drag. The differences between the upstream and downstream pressure coefficients for cases 5 and 6 are 2.48 and 2.31, respectively, which are slightly less than that of the bare riser.

VI. CYLINDRICAL OR GROOVED RISER WITH DIFFERENT STRIP ARRANGEMENTS

This section investigates the details of the uniform flow over the different geometries and seeks the mechanism by which the various

geometries of the flexible riser suppress VIV. Based on the numerical results discussed in Sec. V and by Hu *et al.*,⁴² the installation angles of strips are set in this analysis at 45° and 135° , and the thicknesses are set to $0.08D$ and $0.05D$, respectively.

A. Strip thickness of 0.08D

Figure 16 compares the dimensionless RMS crossflow displacements with the RMS inline displacements along the span of the bare riser and of the six cases (2, 8–12) with a strip thickness of $0.08D$. Table V lists the maximum dimensionless RMS displacement and the corresponding axial positions. As shown in Fig. 16(a), all configurations

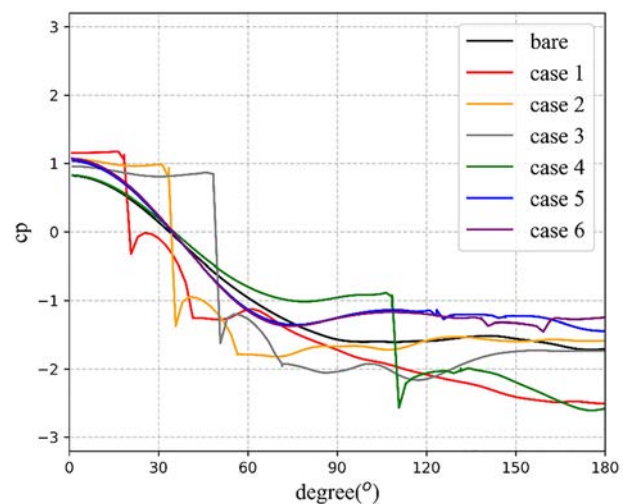


FIG. 15. Pressure distribution of flow past the cross section at the fifth fluid strip.

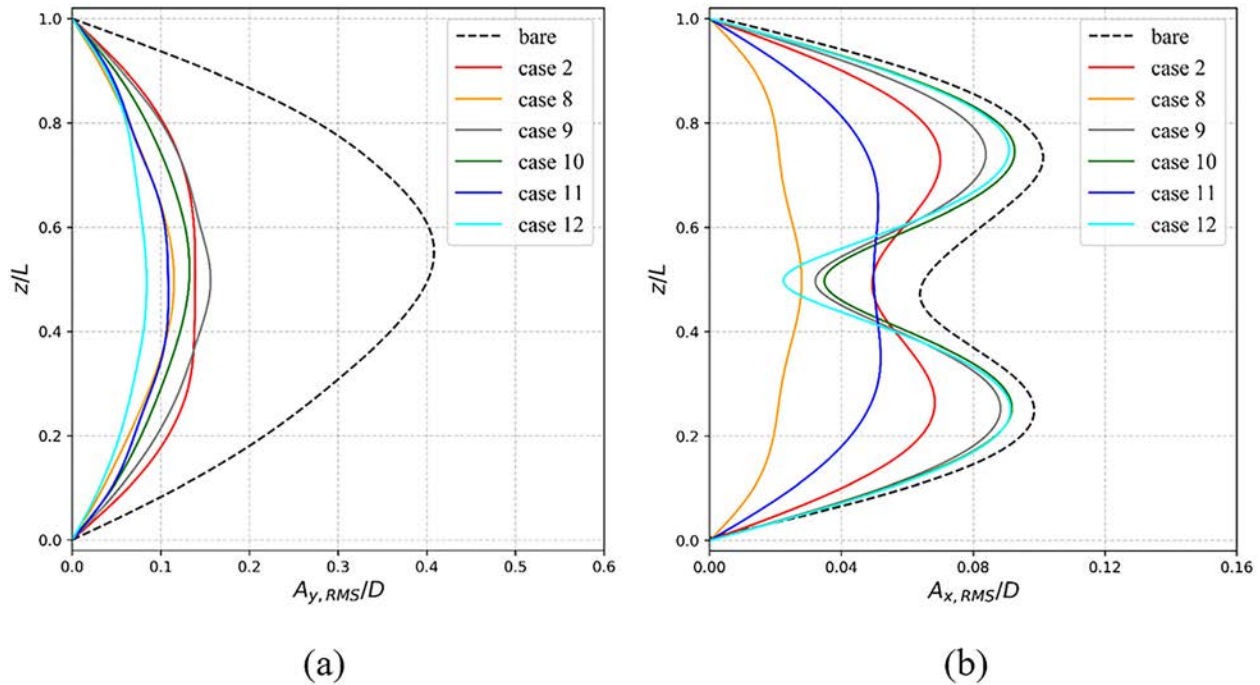


FIG. 16. Dimensionless RMS displacement along riser span. (a) Crossflow, (b) inline.

suppress the dimensionless RMS crossflow displacements and maintain the first-order vibration form, and the axial positions of the maximum RMS crossflow displacement remain close to 0.5L. Case 8, with four spanwise symmetrical strips, better suppresses the dimensionless RMS crossflow displacements than does case 2, with two spanwise symmetrical strips. The maximum dimensionless RMS crossflow displacement is 0.015D, which represents a decrease in 71.7% with respect to the bare riser. The suppression of the maximum dimensionless RMS crossflow displacements of the grooved riser fitted with spanwise symmetrical strips (cases 10 and 11) increases compared with the cylindrical riser fitted with spanwise symmetrical strips (cases 2 and 8), although the further reduction in the maximum dimensionless RMS crossflow displacement (0.132D and 0.108D) is limited and represents a decrease in 67.6% and 73.5% with respect to the bare riser. Moreover, applying the staggered symmetrical strip arrangement to the cylindrical riser (case 9) causes the maximum dimensionless RMS crossflow displacement (0.156D) to decrease by 61.7% with respect to the bare riser, which

is the worst suppression of the six cases. The best suppression of the maximum dimensionless RMS crossflow displacement (0.084D) is for case 12, when the grooved riser is equipped with staggered symmetrical strips; the decrease in this case is 79.3% with respect to the bare riser. The above results show that the introduction of grooves can further enhance VIV inhibition in the crossflow direction, although the effect is different under different strip configurations.

Figure 16(b) shows that, although the six cases suppress to some extent the dimensionless RMS inline displacements, the suppression is mostly limited compared with the crossflow direction. The greatest suppression of the maximum dimensionless RMS inline displacement is for case 8, which causes a decrease in 72.3% (to 0.028D) with respect to the bare riser. However, changing the riser with four symmetrical strips from cylindrical (case 8) to grooved (case 11) increases the maximum dimensionless RMS inline displacement to 0.052D, which is a decrease in 48.5% with respect to the bare riser. A similar situation also occurs for cases 2 and 10. The worst suppression of the maximum dimensionless RMS inline displacement is for cases 9 and 12, which both produce a decrease in less than 18.0% with respect to the bare riser. In addition, the gap between the maximum dimensionless RMS inline displacement of cases 9 and 12 is the smallest. Moreover, unlike the other cases with the second-order vibration form, cases 8 and 11 cause more like a first-order vibration form. In addition, because the two peaks of the second-order vibration form are not completely symmetrical, the axial positions differ for maximum dimensionless RMS inline displacements in the six cases.

Figure 17 shows the crossflow vibration mode weights as functions of time and the corresponding PSDs for cases 8–12. The vibration amplitudes of the first- and second-order crossflow mode of cases 8–12 are both suppressed with respect to that of the bare riser. Case 8,

TABLE V. Maximum dimensionless RMS displacements at the given axial positions.

	Crossflow		Inline	
	$A_{y, RMSmax}/D$	z/L	$A_{x, RMSmax}/D$	z/L
Case 8	0.115	0.495	0.028	0.500
Case 9	0.156	0.500	0.088	0.255
Case 10	0.132	0.520	0.093	0.745
Case 11	0.108	0.465	0.052	0.350
Case 12	0.084	0.495	0.091	0.250

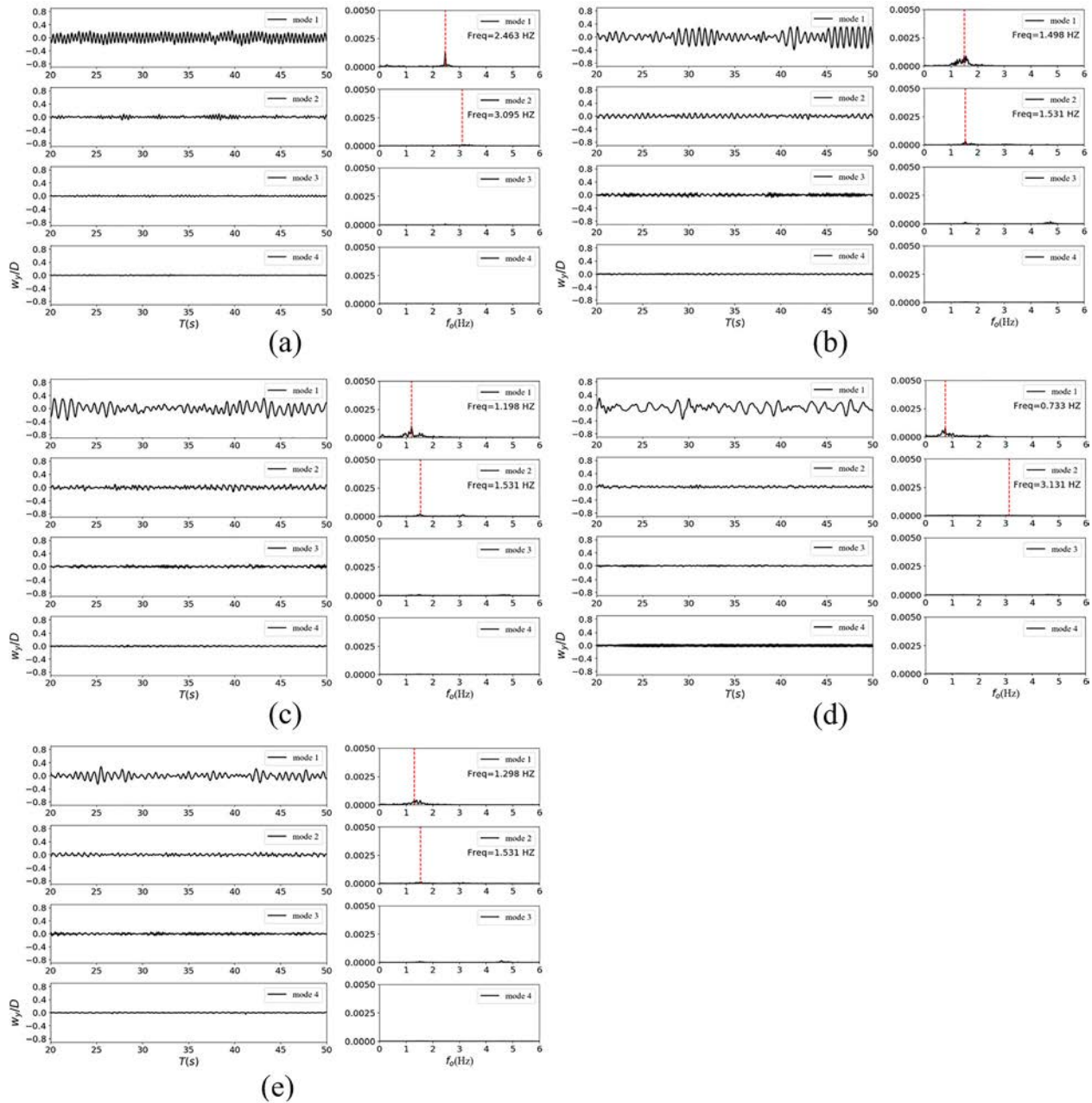


FIG. 17. Crossflow vibration mode weights (w_y/D) as functions of time and the corresponding PSDs. (a) case 8, (b) case 9, (c) case 10, (d) case 11, (e) case 12.

with four symmetrical strips, produces a constant-vibration-amplitude first-order crossflow mode over the time displayed, which differs from the situation for case 2. When the riser changes from cylindrical to grooved, the vibration amplitudes of the first-order crossflow mode for case 11 vary significantly over time in a wave-like pattern. Such wave-like first-order crossflow mode oscillations also appear in cases 9, 10, and 12. The 2.463 Hz frequency of the first-order crossflow mode vibration for case 8, which is similar to the frequency for case 2,

is greater than the corresponding frequency for the bare riser. However, when using a staggered arrangement of symmetrical strips (case 9), the corresponding frequency for case 9 drops to 1.498 Hz, and the addition of the grooved structure (cases 10–12) further decreases the frequency to 1.198, 0.733, and 1.298 Hz, respectively. Furthermore, the peak PSDs for cases 8–12 are lower than that of the bare riser, and the first-order crossflow mode vibration frequencies are not concentrated for cases 9–12. The above results show that both the

staggered strips and the grooves are beneficial to the reduction of the crossflow mode vibration frequency and eliminate the risk of causing high-order mode vibration in the crossflow direction, but crossflow mode vibration frequency of staggered strips with no grooves is closer to the first-order natural frequency, and it is easier to excite a relatively higher crossflow amplitude.

Figure 18 shows the inline vibration mode weights as functions of time and the corresponding PSDs for cases 8–12. The amplitudes of

the third-order inline mode vibrations for cases 8–12 are both suppressed with respect to the bare riser. Figure 18(a) shows that the suppression of the amplitude of the second-order inline mode vibration remains constant over time. For case 8, the amplitude of the vibration frequencies of the second-order inline mode is much less than that for the bare riser. The situation of case 9, which uses a staggered arrangement of symmetrical strips, is similar to that of case 2, whose vibrational amplitudes of the inline mode decrease and the corresponding

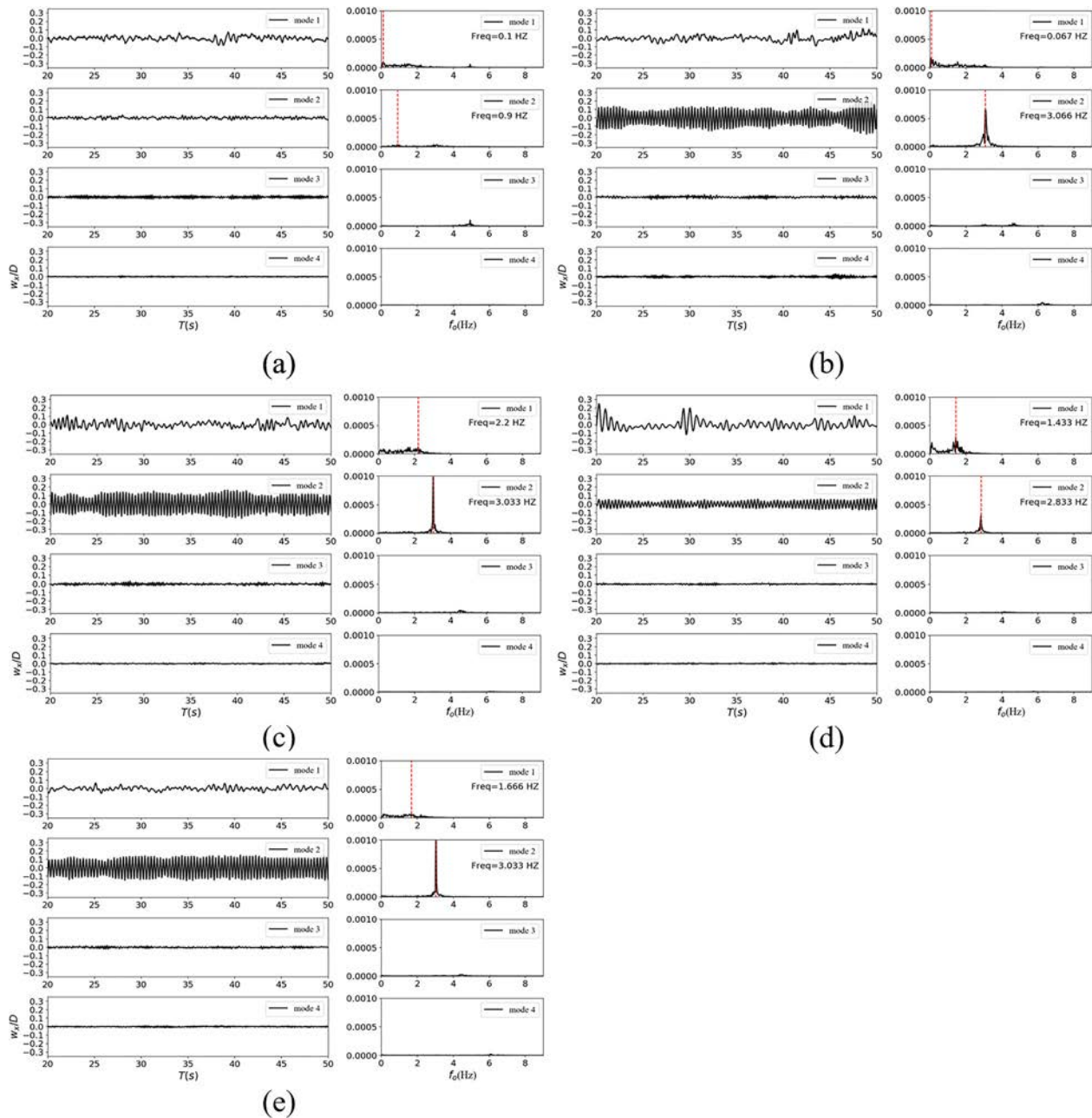


FIG. 18. Inline vibration mode weights (w_x/D) as functions of time and the corresponding PSDs. (a) case 8, (b) case 9, (c) case 10, (d) case 11, (e) case 12.

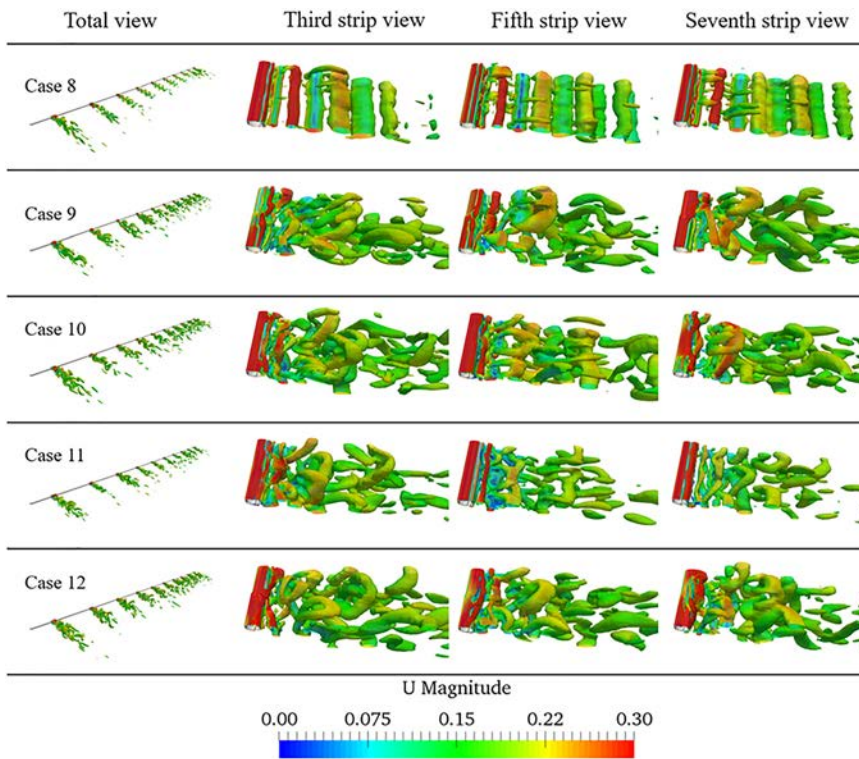


FIG. 19. Instantaneous vortex structures through the Q criterion ($Q = 5$) of three fluid strips for cases 8–12 at 47 s; from left to right: total, third strip, fifth strip, and seventh strip.

frequencies approach those of the bare riser. Case 11 involves a grooved riser on which symmetrical strips are fixed, and the amplitudes of both the first- and second-order inline modes are enhanced with respect to case 8, and the corresponding inline mode vibration frequencies increase to 1.433 and 2.833 Hz, respectively. The corresponding first-order inline mode vibration frequencies increase from 0.067 to 1.666 Hz for cases 9 and 12, which is similar to the situation in going from case 2 to case 10. This implies that the grooved structure may increase the vibration frequencies of the first-order inline mode.

Figures 19 and 20 show the instantaneous 3D vortex structures and the instantaneous 2D vortex shedding for cases 8–12. As the attached spanwise bi-symmetrical strips (case 2) become spanwise four-symmetrical strips (case 8), and the wavy- and smaller discrete-type vortex structures nearly disappear from the 3D vortex structures at different positions for the fluid strips displayed, indicating that the strips installed at the tail in case 8 lost the role of discrete wake regions.

The 3D vortex structures are consistent along the riser span and are almost completely dominated by cylindrical-type vortex structures, bringing an increase in crossflow vibration frequency. When the symmetrical strips are staggered (case 9), the discontinuity of the strip structures in the spanwise direction breaks the consistency of the 3D vortex structures in the spanwise direction and induces a decrease in crossflow vibration frequency. The third, fifth, and seventh fluid strips both produce wavy- and smaller discrete-type vortex structures, whereas no cylindrical-type vortex structures exist. By introducing grooves on the riser surface (cases 10–12), the 3D vortex structures from the different fluid strips are similar to those produced by the staggered symmetrical strips: only scattered twisted cylindrical-type vortex structures appear at the fifth fluid strips for cases 10 and 11, and all fluid strips are dominated by the wavy- and smaller discrete-type vortex structures, meaning a decrease in crossflow vibration frequency.

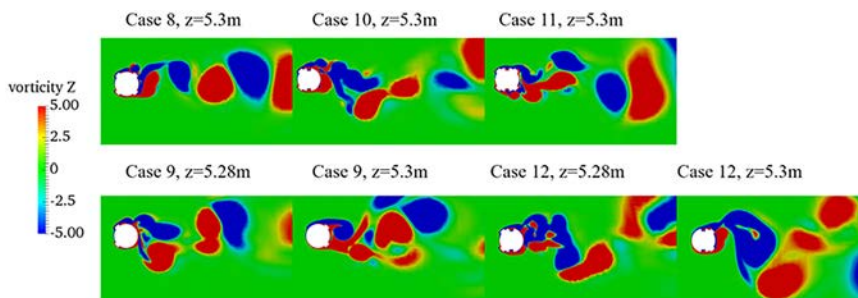


FIG. 20. Instantaneous z vorticity for cases 8–12 at 46 s.

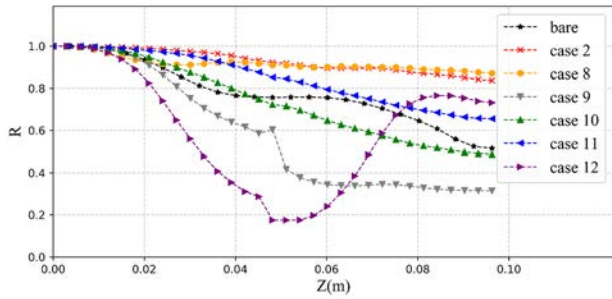


FIG. 21. Correlation coefficient R of lift at the fifth fluid strip as a function of position z .

Figure 20 shows that case 8 sheds regular rows of 2D vortices whose rotational directions reverse over time. At $z = 5.28$ and 5.3 m, irregular 2D vortices are generated in a staggered arrangement (case 9), but the number of vortices and the width of the vortex street increase with respect to cases 2 and 8. By introducing grooves on the riser surface (case 11), unlike case 8, the presence of opposite vortices inside the grooves renders irregular the shredded 2D vortices, with some smaller vortices produced. Meanwhile, similar to the change from case 2 to 10, the main difference of cases 9 and 12 is that they generate smaller vortices in the wake region.

Figure 21 shows the correlation coefficient R of the lift along the span of the fifth fluid strip for the bare riser, cases 2,⁴² and 8–12. For case 8, the drop of the correlation coefficient for lift along the span is slightly less than for case 2, which verifies that, for case 8, the 3D vortex structures along the spanwise direction are more consistent than for case 2. Given that the symmetrical strips of the two structural elements included in the fifth fluid strip are installed in different positions for case 9, the relative decrease in the correlation coefficient R of lift in

the spanwise direction is greater than that for cases 2 and 8, which means that the 3D vortex structure is more discrete for case 9. This explains the sudden drop in the correlation coefficient R of lift at the junction of the two structural elements. After the groove structure is introduced, the drop of the correlation coefficients of lift for cases 10 and 11 increases with respect to cases 2 and 8, explaining the transition of the 3D vortex structure of case 11 vis à vis case 8. Unlike the other cases, the correlation coefficient of lift for case 12 decreases the most along the spanwise direction of the lower structural elements of the fifth fluid strip but also increases significantly along the spanwise direction of the upper structural elements of the fifth fluid strip. This result shows that the correlation coefficient R of lift for case 12 is the worst of all cases displayed in Fig. 21, which implies that the 3D vortex structures for case 12 are highly dispersed.

Figure 22 shows the skin friction as a function of peripheral angle of the cross section for cases 2⁴² and 8–12. For case 8, the strips on both the leading and trailing edges of the cross section produce two forced separation points at around 45° and 135° , whereas the reattachment point of case 2 disappears, which means that flow separation is delayed to around 135° for case 8, thereby delaying the formation of vortices. For case 11, the circular section is grooved, so a secondary forced separation (Φ_{fss}) point appears near the groove structure, and the flow breaks up in the groove to form small vortices, which can be seen in Fig. 20. At the same time, a third forced separation point (Φ_{fs}) appears at the trailing edge near 135° , so the variation of the shear stress is very complicated, which leads to a complex flow on the riser surface and affect the stability of the periodic variation of the wake region. Therefore, although the variation of the shear stress for case 10 is close to that for case 2, the flow for case 10 with the groove structure is more complex, and the variation of the shear stress in the lower structural elements in going from case 9 to 12 is similar to that in going from case 2 to 10. The cross-sectional shear stress of the upper

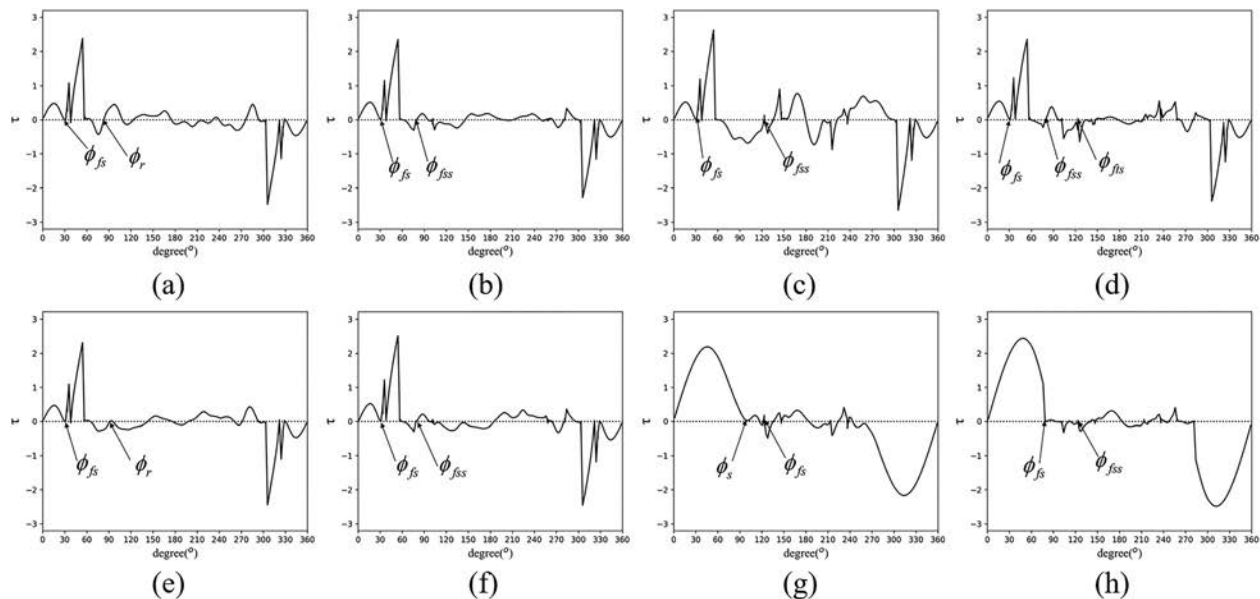


FIG. 22. Distribution of skin friction along peripheral angle of cross section at the fifth fluid strip. (a) case 2; (b) case 10; (c) case 8; (d) case 11; (e) case 9, lower elements; (f) case 12, lower elements; (g) case 9, upper elements; (h) case 12, upper elements.

structural elements of case 12 differs from that of case 9 in that the former drops sharply at the grooves around 90° , where the flow forms the forced separation.

Figures 23(a) and 23(b) compare the pressure distribution of the flow over the different cross sections of the bare riser, case 2,⁴² and cases 8–12 at the fifth fluid strip. The surface pressure of cases 2, 8, 10, and 11 is concentrated at unity at the front most point. Cases 2 and 8 then both experience similar changes in surface pressure at the leading edge of the strip, with the recovery of the surface pressure in case 8 being significantly greater than that in case 2, and the pressure coefficient of case 8 reaches -1.0 . With the appearance of the trailing edge strip, the surface pressure of case 8 enters a downward trend, and the final surface pressure is lower than that of case 2, which means that the total drag increases. For cases 10 and 11, the viscous sublayer breaks at the groove structure around 90° and the velocity gradient disappears, so the pressure coefficient remains constant at approximately -1.5 , which differs from the pressure distribution at the same position for cases 2 and 8. Then, the surface pressure for cases 10 and 11 basically follows an upward trend, with the final surface pressure exceeding that of cases 2 and 8, which indicates that the groove structure reduces the total drag. Figure 23(b) shows that, although the surface pressure distributions at the front-most point are similar for cases 9 and 12, they differ at the upper and lower structural elements because of the different cross sections of the two cases. Case 12 experiences an almost-constant pressure distribution at the groove structure. The final surface pressures at the upper and lower structural elements of case 12 are greater than those of the corresponding structural elements of case 9, indicating that the structural configuration of case 12 reduces the total drag with respect to case 9.

B. Strip thickness of 0.05D

Figure 24 compares the dimensionless RMS crossflow and the RMS inline displacements along the span of the bare riser and along

the risers of six different cases with a strip thickness of $0.05D$. Table VI lists the maximum dimensionless RMS displacement along with the corresponding axial positions. Although the dimensionless RMS crossflow displacements are suppressed for cases 13–17, case 15 produces a second-order mode form like case 7.⁴² Thus, the axial positions for the maximum dimensionless RMS crossflow displacements of cases 15 and 7 differ from those of the other cases displayed in Fig. 24. Like the cases with the thickness of $0.08D$, the maximum dimensionless RMS crossflow displacement for case 13 with $0.132D$ further decreases compared with that of case 7 with $0.215D$ (the decrease goes from 47.2% to 67.6%, respectively, with respect to the bare riser). Upon introducing the groove structure, the maximum dimensionless RMS crossflow displacement for case 15 is less than that of case 7, with a decrease 63.9% with respect to the bare riser. The maximum dimensionless RMS crossflow displacement for case 16 is slightly greater than that of case 13, with a decrease in 61.4% with respect to the bare riser. Like the variation from case 9 to case 12 when the strip thickness is $0.08D$, the suppression of the dimensionless RMS crossflow displacement goes from relatively poor (case 14) to the best (case 17), with decreases of 47.9% and 83.8% for cases 14 and 17, respectively, with respect to the bare riser. For the same structural configuration, the suppression of the dimensionless RMS crossflow displacement for case 17 is slightly better than that of case 12. Therefore, except for case 13, the introduction of the groove structure strengthens VIV suppression, and, when the strip thickness decreases from $0.08D$ to $0.05D$, the variation of the structural configuration exerts an increased effect on the dimensionless RMS crossflow displacement.

Figure 24(b) shows that the dimensionless RMS inline displacements are suppressed for cases 13–17. However, due to the different arrangement of the symmetrical strips, case 13 produces a third-order vibration form, whereas case 14 produces a second-order vibration form, which both differ from the first-order vibration form produced by case 7. The best suppression occurs in case 13, and the maximum dimensionless RMS inline displacement is $0.028D$, which is a 72.3%

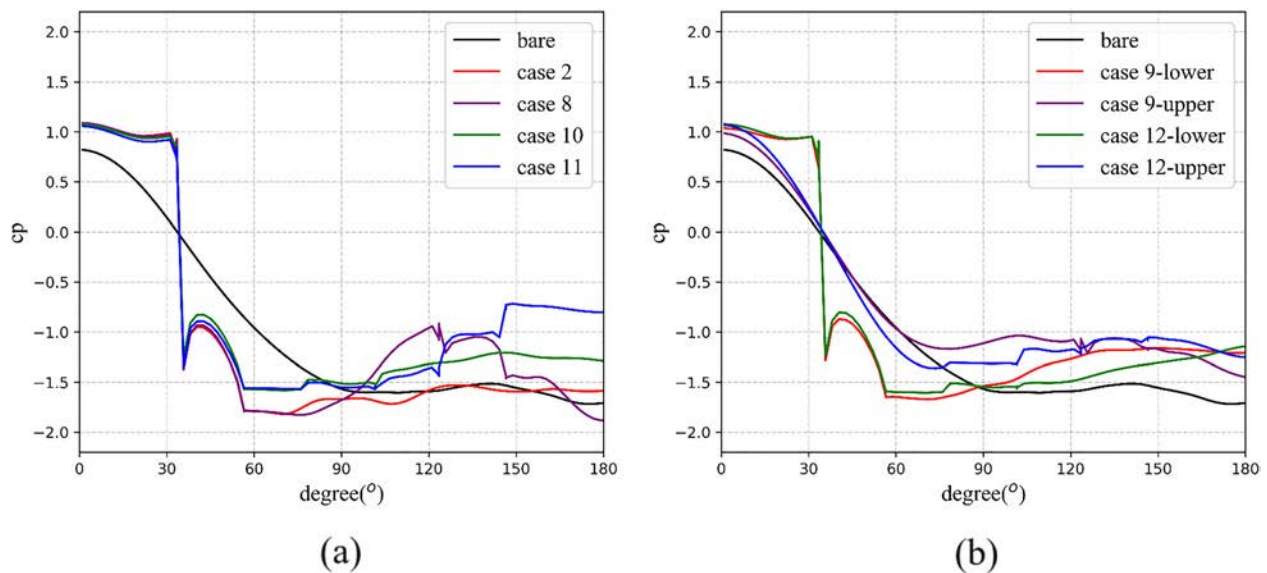


FIG. 23. Pressure distribution of flow over cross section at the fifth fluid strip. (a) Spanwise, (b) staggered.

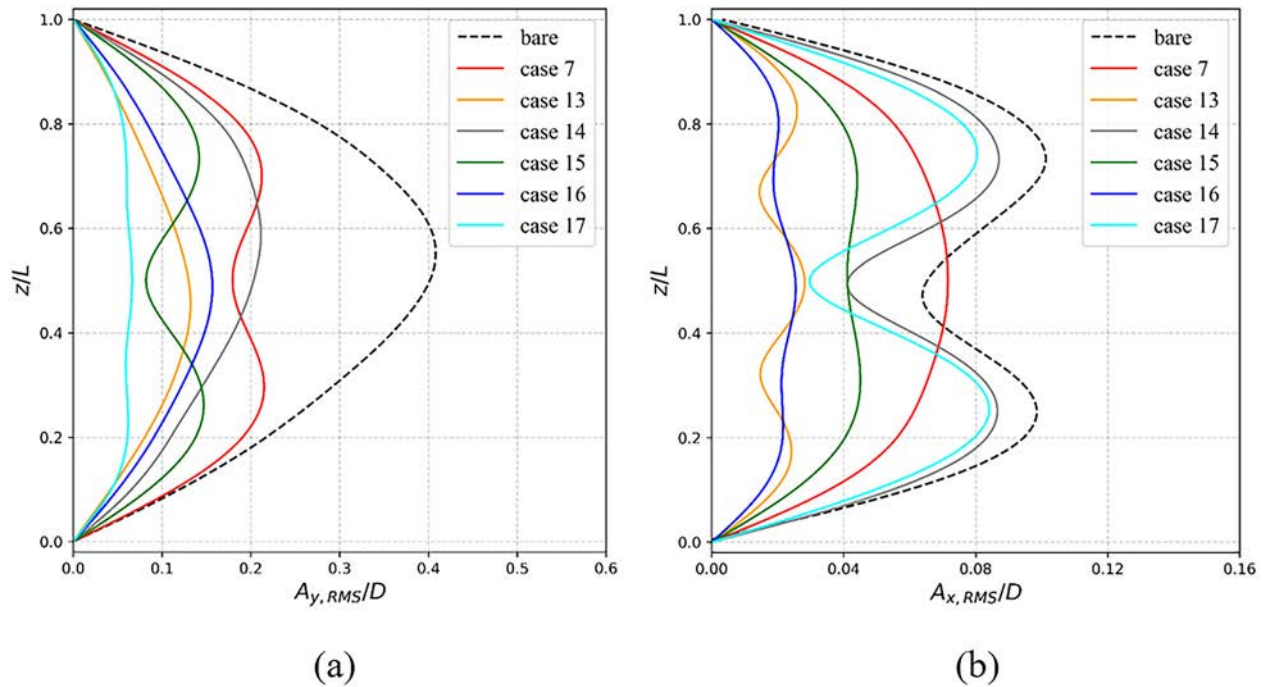


FIG. 24. Dimensionless RMS displacement along riser span. (a) Crossflow, (b) inline.

decrease with respect to the bare riser. As opposed to the cases where the strip thickness is 0.08D, the introduction of the groove structure results in a maximum dimensionless RMS inline displacement of case 16 (0.025D) being close to that of case 13, with the decrease being 75.2% with respect to the bare riser. The same situation occurs for case 17, for which the maximum dimensionless RMS inline displacement (0.084D) is close to that of case 14. However, the variation in the maximum dimensionless RMS inline displacement for cases 15 and 7 is relatively large compared with that of the bare riser: the decrease is 29.7% for case 7 and 55.4% for case 15 with respect to the bare riser.

Figure 25 shows the crossflow vibration mode weights as functions of time and the corresponding PSDs for cases 7⁴² and 13–17. Compared with the bare riser, cases 13, 14, 16, and 17 all suppress to some extent the vibration amplitudes of the first- and second-order crossflow modes. For case 15, the vibration amplitudes of the second-

order crossflow mode and the corresponding frequencies are enhanced, which is like case 7. Unlike the wave-like vibration mode in the other cases of Fig. 25, cases 13 and 16 both produce constant vibration amplitudes for the first-order crossflow mode, and the corresponding frequency for case 16 (2.396 Hz) is slightly greater than that of case 13 (2.196 Hz). Moreover, the corresponding frequency for case 17 (1.498 Hz) is less than that of case 14 (1.564 Hz), and the frequencies of cases 14 and 17 are both less than that of the bare riser. Compared with similar configurations for a strip thickness of 0.08D, these results indicate that the groove structure has less effect on the crossflow mode vibration frequencies for the cases of Fig. 25.

Figure 26 shows the inline vibration mode weights as functions of time and the corresponding PSDs for cases 7⁴² and 13–17. The vibration amplitudes of the second-order inline mode are suppressed for cases 13, 15, and 16. For cases 13 and 16, the vibration amplitudes of the third-order inline mode are greater than those of the other orders, and the corresponding frequency for case 16 (4.799 Hz) is slightly greater than that for case 13 (4.399 Hz). Compared with case 7, the corresponding peak at the second-order inline mode vibration frequency for case 15 is relatively high, whereas the relatively small peak of the second-order inline mode vibration frequency disappears. Moreover, the decrease in the vibration amplitudes of the second-order inline modes of cases 14 and 17 are limited in comparison with that of the bare riser, and the corresponding frequency for case 17 (3.099 Hz) is slightly less than that for case 14 (3.199 Hz). Therefore, unlike varying the strip arrangement, adding a groove structure generally produces little effect on inline mode vibration frequencies for the cases of Fig. 26.

Figures 27 and 28 show the instantaneous 3D vortex structures and the instantaneous 2D vortex shedding for cases 7⁴² and 13–17. Similar to the situation shown in Fig. 19 for 0.08D, the arrangement

TABLE VI. Maximum dimensionless RMS displacements and the corresponding axial positions.

	Crossflow		Inline	
	$A_{y, RMSmax}/D$	z/L	$A_{x, RMSmax}/D$	z/L
Case 7 ⁴²	0.215	0.295	0.071	0.500
Case 13	0.132	0.455	0.028	0.495
Case 14	0.212	0.585	0.087	0.735
Case 15	0.147	0.260	0.045	0.310
Case 16	0.157	0.490	0.025	0.485
Case 17	0.066	0.500	0.084	0.255

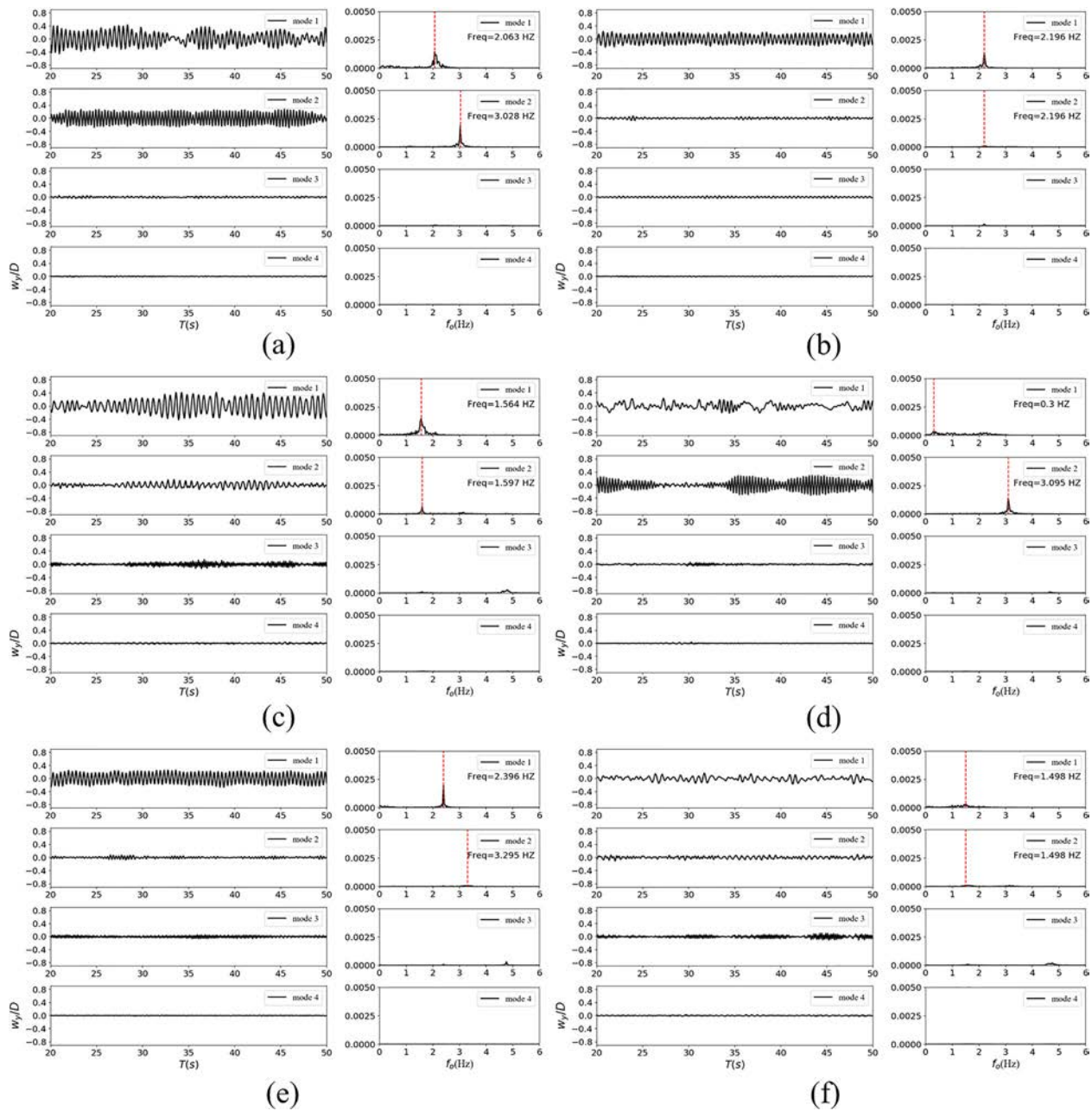


FIG. 25. Crossflow vibration mode weights (w_y/D) as functions of time and the corresponding PSDs. (a) Case 7, (b) case 13, (c) case 14, (d) case 15, (e) case 16, (f) case 17.

of the four symmetrical spanwise strips (case 13) helps to form cylindrical-type vortex structures with fine axial consistency, whereas the arrangement of four staggered symmetrical strips [case 14] is more likely to form wavy-type and smaller, discrete-type vortex structures with strong 3D features. Additionally, comparing case 8 in Fig. 19 with case 13 in Fig. 27 shows that, as the thickness of the strip decreases, more wavy- and smaller discrete-type vortex structures form, indicating that the consistency of the 3D vortex structures decreases. Applying grooves to the surface of the riser (case

16) produces no great change in the vortex structures compared to case 13, unlike going from cases 8 to 11, which indicates that reducing the strip thickness decreases the influence of the grooves on the 3D vortex structures. In addition, the combination of four staggered symmetrical strips and the grooves still produces the most disperse 3D vortex structures. Consistent with the performance of the 3D vortex structures, cases 13 and 16 produce more regular 2D vortices, whereas cases 14 and 17 produce more irregular 2D vortices.

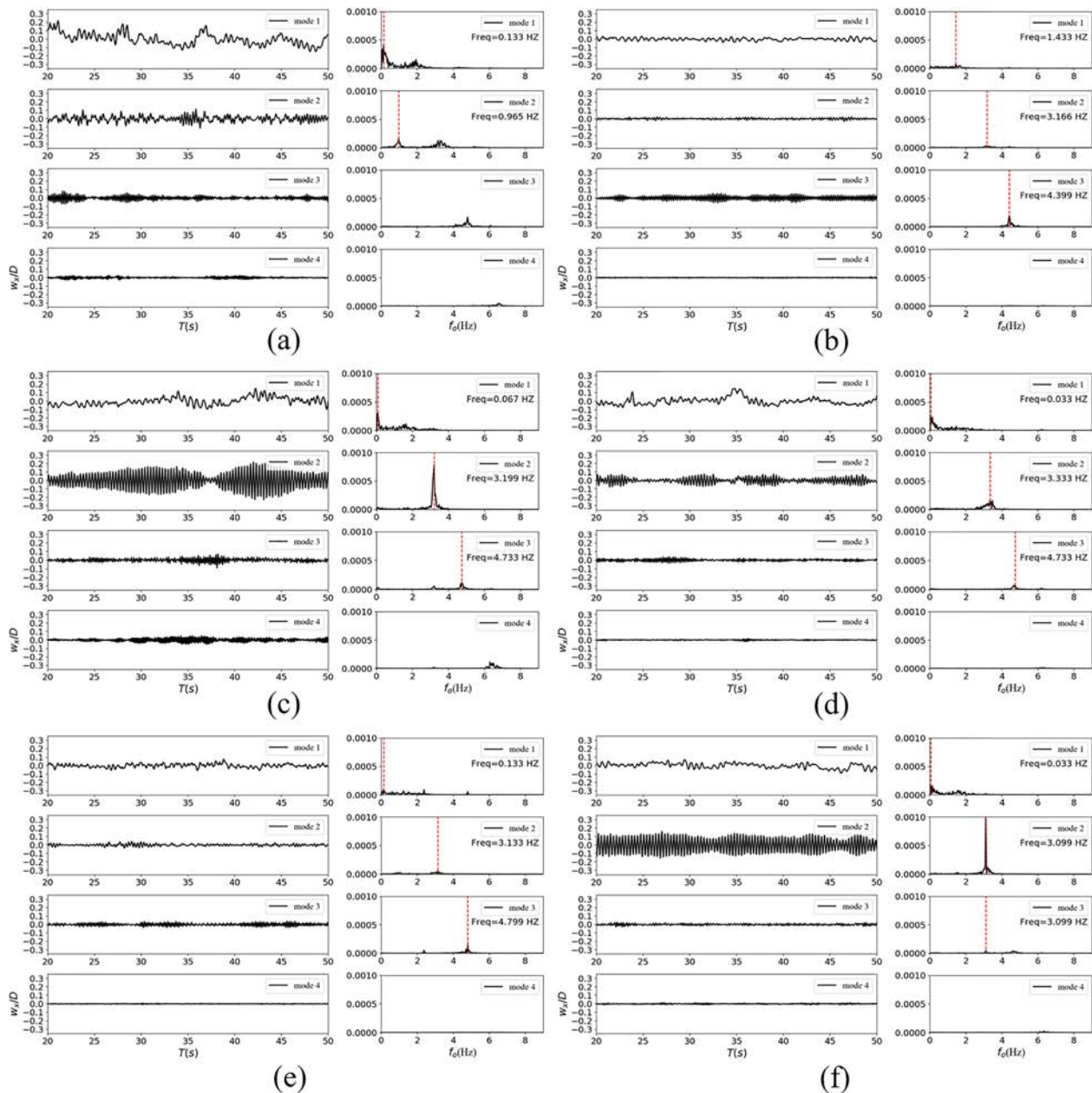


FIG. 26. Inline vibration mode weights (w_x/D) as functions of time and the corresponding PSDs. (a) Case 7, (b) case 13, (c) case 14, (d) case 15, (e) case 16, (f) case 17.

VII. CONCLUSIONS

This paper numerically investigates the VIV of cylindrical or grooved slender flexible risers with strips symmetrically installed on their surface. The devices are exposed to uniform flow at a fixed velocity, and the simulations are done by using our in-house software viv3D-FOAM-SJTU. The simulations consider two positions of the spanwise symmetrical strips, and cylindrical and grooved risers, both with two spanwise symmetrical strips attached, four spanwise symmetrical strips attached, or four staggered symmetrical strips attached. We

also compare two strip thicknesses (0.05D and 0.08D). Based on an analysis of the dimensionless RMS displacements, modal weights, PSDs, 2D and 3D wake flow field, lift correlation, and pressure and skin friction distributions of the different configurations, the following conclusions are drawn:

- (1) The VIV of the cylindrical riser depends on the angle of the two spanwise symmetrical strips. The strips installed at $\alpha = 45^\circ$, 135° , and 150° suppress the RMS displacements in the cross-flow direction, the maximum RMS displacements decreasing by

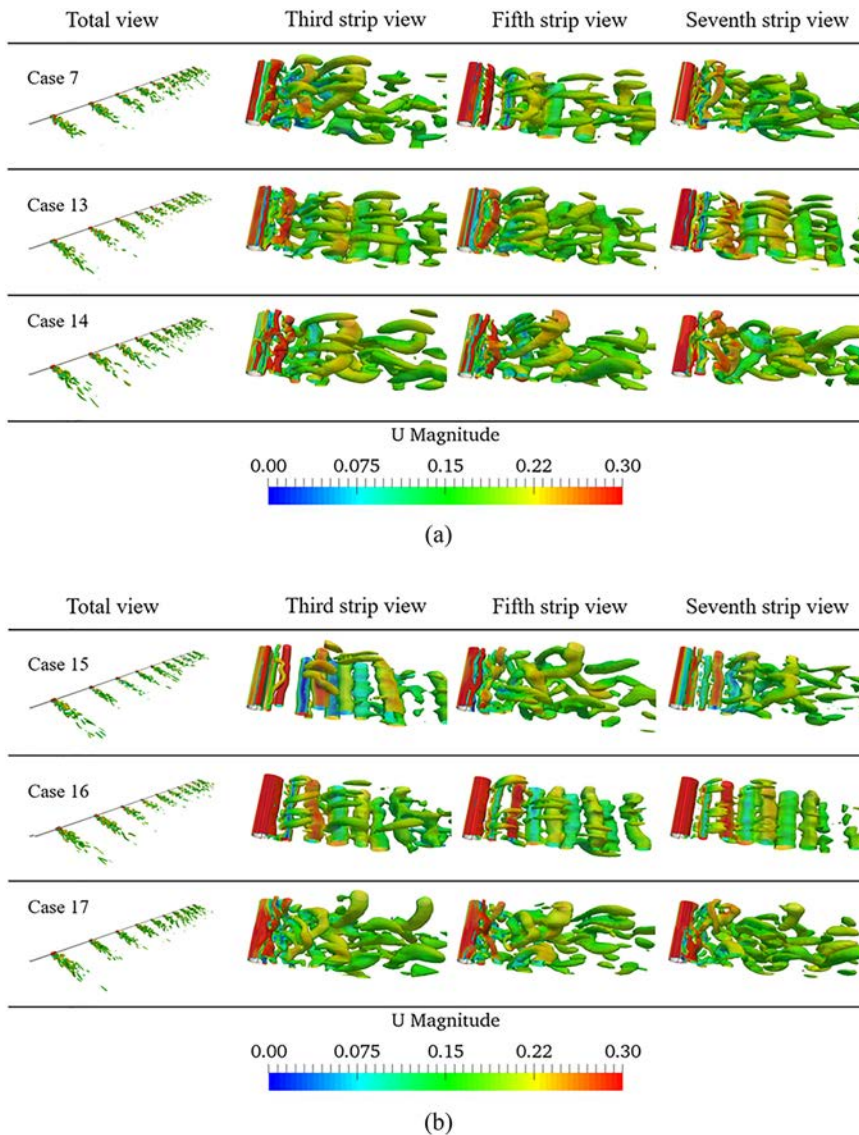


FIG. 27. Instantaneous vortex structures through the Q criterion ($Q = 5$) of three fluid strips for (a) cases 7, 13, and 14, (b) cases 15–17 at 47 s; from left to right: total, third, fifth, and seventh strip.

65.8%, 60.2%, and 65.1% with respect to the bare riser. In contrast, the maximum RMS displacement in the crossflow direction for $\alpha = 60^\circ$ increases by 49.4% with respect to the bare riser. The different strip angles cause complex variations in the

vibration form of the RMS displacements in the inline direction, thereby complicating the changes in the axial position and in the maximum RMS displacement. Moreover, the vibration frequencies corresponding to the first-order crossflow mode of

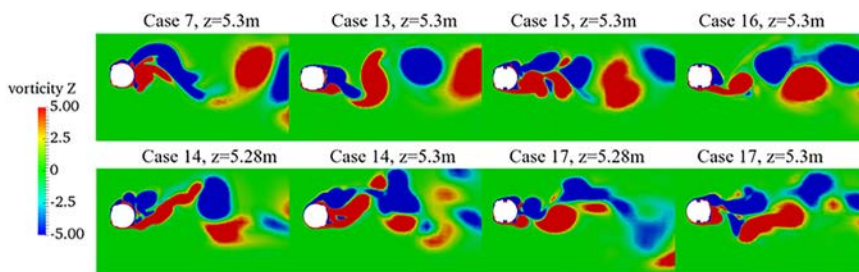


FIG. 28. Instantaneous z vorticity for cases 7 and 13–17 at 46 s.

the riser with two spanwise symmetrical strips at $\alpha = 30^\circ$ and 45° are greater than that of the bare riser, whereas the corresponding frequencies of the riser with two spanwise symmetrical strips at $\alpha = 135^\circ$ and 150° are less than that of the bare riser.

- (2) For two spanwise symmetrical strips installed at $\alpha = 30^\circ$ and 45° , the distribution of skin friction force shows that, due to the presence of a reattachment point, the separation of the boundary layer is delayed to bring VIV inhibition, but the riser experiences strongly correlated lift, so that it suffers from more cylindrical-type vortex structures, increment of crossflow vibration frequency, regular vortex shedding, and more total drag. However, flow separation occurs earlier because no secondary attachment points form for $\alpha = 60^\circ$, which enhances the VIV for case 3. Given that the installation angle is defined at the trailing edge of the riser, the two spanwise symmetrical strips mainly divide the wake region to suppress VIV, and lead to relatively weak lift correlation, more wavy- and small discrete-type vortex structures, decrement of crossflow vibration frequency, irregular vortex shedding.
- (3) For a strip thickness of $0.08D$, the cylindrical riser produces the better suppression of the RMS displacements in the crossflow direction when using four spanwise symmetrical strips. The maximum decrease in RMS displacement is 71.7% with respect to the bare riser. Adding a grooved structure on the riser surface improves the suppression effect, and the grooved riser with four staggered symmetrical strips makes for the best suppression of all configurations, with a maximum decrease in RMS displacement of 79.3% with respect to the bare riser. In addition, the vibration frequencies corresponding to the first-order crossflow mode of the grooved riser also decrease compared with the same configuration of the cylindrical riser. Varying the number of strips and adding grooves produces a complex effect on the mode vibrations and the RMS displacements in the inline direction.
- (4) Attaching four spanwise symmetrical strips of thickness $0.08D$ to the surface of a cylindrical riser produces a skin friction force distribution that delays separation of the boundary layer to the trailing-edge strip to enhance the VIV suppression effect. However, the lift correlation in this case is greater than that for two spanwise symmetrical strips, and cylindrical-type vortices and regular vortex shedding dominate the wake region, bringing an increase in crossflow vibration frequency. Introduction of the grooved structure on the surface of a riser symmetrical strips brings a complex flow on the riser surface to affect the stability of the periodic variation of the wake region, which ameliorates the VIV suppression effect, mainly in can decrease the lift correlation, produce more wavy- and small, discrete-type vortices, increase shedding of irregular vortices, and reduce the crossflow vibration frequency. In addition, the total drag force decreases compared with the original cylindrical riser.
- (5) For a strip thickness of $0.05D$, the configuration with a grooved riser to which are attached four staggered symmetrical strips still produces the best suppression of RMS displacements in the crossflow direction, with a decrease of 83.8% with respect to the bare riser. Changing the configuration also causes complex variations in the RMS displacements in the inline direction.

Finally, the grooved structure weakly affects the wake region, especially for four spanwise symmetrical strips.

ACKNOWLEDGMENTS

This work was supported by the National Key Research and Development Program of China (Grant No. 2019YFB1704200) and the National Natural Science Foundation of China (Grant Nos. 52131102 and 51879159), to which the authors are most grateful.

AUTHOR DECLARATIONS

Conflict of Interest

The authors have no conflicts to disclose.

Author Contributions

Hao Hu: Data curation (equal); Investigation (equal); Methodology (equal); Software (equal); Validation (equal); Visualization (equal); Writing – original draft (equal). **Weiwu Zhao:** Data curation (equal); Formal analysis (equal); Investigation (equal); Methodology (equal); Software (equal); Validation (equal); Writing – original draft (equal). **Decheng Wan:** Conceptualization (equal); Funding acquisition (equal); Methodology (equal); Software (equal); Supervision (equal); Writing – review & editing (equal).

DATA AVAILABILITY

The data that support the findings of this study are available from the corresponding author upon reasonable request.

REFERENCES

- ¹R. D. Blevins, *Flow-Induced Vibration* (Van Nostrand Reinhold, 1977).
- ²J. R. Chaplin, P. W. Bearman, F. J. Huera Huarte *et al.*, “Laboratory measurements of vortex-induced vibrations of a vertical tension riser in a stepped current,” *J. Fluids Struct.* **21**, 3–24 (2005).
- ³J. R. Chaplin and R. King, “Laboratory measurements of the vortex-induced vibrations of an un tensioned catenary riser with high curvature,” *J. Fluids Struct.* **79**, 26–38 (2018).
- ⁴Y. Duanmu, L. Zou, and D. C. Wan, “Numerical simulations of vortex-induced vibrations of a flexible riser with different aspect ratios in uniform and shear currents,” *J. Hydrodyn.* **29**(6), 1010–1022 (2017).
- ⁵Y. Duanmu, L. Zou, and D. C. Wan, “Numerical analysis of multi-modal vibrations of a vertical riser in step currents,” *Ocean Eng.* **152**, 428–442 (2018).
- ⁶K. S. Hong and U. H. Shah, “Vortex-induced vibrations and control of marine risers: A review,” *Ocean Eng.* **152**, 300–315 (2018).
- ⁷J. Wang, D. Fan, and K. Lin, “A review on flow-induced vibration of offshore circular cylinders,” *J. Hydrodyn.* **32**(3), 415–440 (2020).
- ⁸W. L. Chen, Y. Huang, C. Chen *et al.*, “Review of active control of circular cylinder flow,” *Ocean Eng.* **258**, 111840 (2022).
- ⁹F. C. Hebrero, J. D’Adamo, R. Sosa *et al.*, “Vortex induced vibrations suppression for a cylinder with plasma actuators,” *J. Sound Vib.* **468**, 115121 (2020).
- ¹⁰H. Wang, L. Ding, L. Zhang *et al.*, “Control of two-degree-of-freedom vortex induced vibrations of a circular cylinder using synthetic jets: Effect of synthetic jet orientation angle and phase difference,” *Ocean Eng.* **217**, 107906 (2020).
- ¹¹H. Wan and S. S. Patnaik, “Suppression of vortex-induced vibration of a circular cylinder using thermal effects,” *Phys. Fluids* **28**(12), 123603 (2016).
- ¹²H. Zhu and Y. Gao, “Vortex-induced vibration suppression of a main circular cylinder with two rotating control rods in its near wake: Effect of the rotation direction,” *J. Fluids Struct.* **74**, 469–491 (2017).
- ¹³A. Roshko, “On the drag and shedding frequency of two-dimensional bluff bodies,” NACA Technical Report No. TN-3169, 1954.

- ¹⁴R. Abdi, N. Rezazadeh, and M. Abdi, "Investigation of passive oscillations of flexible splitter plates attached to a circular cylinder," *J. Fluids Struct.* **84**, 302–317 (2019).
- ¹⁵Z. Hu, J. Wang, Y. Sun *et al.*, "Flow-induced vibration suppression for a single cylinder and one-fixed-one-free tandem cylinders with double tail splitter plates," *J. Fluids Struct.* **106**, 103373 (2021).
- ¹⁶Y. Z. Law and R. K. Jaiman, "Wake stabilization mechanism of low-drag suppression devices for vortex-induced vibration," *J. Fluids Struct.* **70**, 428–449 (2017).
- ¹⁷G. R. S. Assi, P. W. Bearman, and M. A. Tognarelli, "On the stability of a free-to-rotate short-tail fairing and a splitter plate as suppressors of vortex-induced vibration," *Ocean Eng.* **92**, 234–244 (2014).
- ¹⁸H. Zhu, Z. Liao, Y. Gao *et al.*, "Numerical evaluation of the suppression effect of a free-to-rotate triangular fairing on the vortex-induced vibration of a circular cylinder," *Appl. Math. Model.* **52**, 709–730 (2017).
- ¹⁹W. Wang, B. W. Song, Z. Y. Mao *et al.*, "Numerical investigation on vortex-induced vibration of bluff bodies with different rear edges," *Ocean Eng.* **197**, 106871 (2020).
- ²⁰J. F. Derakhshandeh and N. Gharib, "Numerical investigations on the flow control over bumped surface circular cylinders," *Ocean Eng.* **240**, 109943 (2021).
- ²¹L. Tang, H. Yao, Z. Huang *et al.*, "How wavelike bumps mitigate the vortex-induced vibration of a drilling riser," *J. Comput. Appl. Math.* **7**(3), 1413–1424 (2021).
- ²²J. Wang, S. Sun, L. Tang *et al.*, "On the use of metasurface for vortex-induced vibration suppression or energy harvesting," *Energy Convers. Manag.* **235**, 113991 (2021).
- ²³L. K. Quen, A. Abu, N. Kato *et al.*, "Performance of two-and three-start helical strakes in suppressing the vortex-induced vibration of a low mass ratio flexible cylinder," *Ocean Eng.* **166**, 253–261 (2018).
- ²⁴T. Ishihara and T. Li, "Numerical study on suppression of vortex-induced vibration of circular cylinder by helical wires," *J. Wind Eng. Ind. Aerodyn.* **197**, 104081 (2020).
- ²⁵Y. Ma, W. Xu, H. Ai *et al.*, "The effect of time-varying axial tension on VIV suppression for a flexible cylinder attached with helical strakes," *Ocean Eng.* **241**, 109981 (2021).
- ²⁶H. Baek and G. E. Karniadakis, "Suppressing vortex-induced vibrations via passive means," *J. Fluids Struct.* **25**(5), 848–866 (2009).
- ²⁷W. Wang, Z. Mao, B. Song *et al.*, "Numerical investigation on vortex-induced vibration suppression of the cactus-inspired cylinder with some ribs," *Phys. Fluids* **33**(3), 037127 (2021).
- ²⁸S. Huang, "VIV suppression of a two-degree-of-freedom circular cylinder and drag reduction of a fixed circular cylinder by the use of helical grooves," *J. Fluids Struct.* **27**(7), 1124–1133 (2011).
- ²⁹Y. Z. Law and R. K. Jaiman, "Passive control of vortex-induced vibration by spanwise grooves," *J. Fluids Struct.* **83**, 1–26 (2018).
- ³⁰G. Zhao, J. Xu, K. Duan *et al.*, "Numerical analysis of hydroenergy harvesting from vortex-induced vibrations of a cylinder with groove structures," *Ocean Eng.* **218**, 108219 (2020).
- ³¹C. H. Ma, W. W. Zhao, and D. C. Wan, "Numerical investigations of three-dimensional flows around a cylinder attaching with symmetric strips," *Phys. Fluids* **33**(7), 075101 (2021).
- ³²C. H. Ma, W. W. Zhao, and D. C. Wan, "Numerical investigations of the flow-induced vibration of a three-dimensional circular cylinder with various symmetric strips attached," *Phys. Fluids* **34**, 065102 (2022).
- ³³D. Deng, W. W. Zhao, and D. C. Wan, "Vortex-induced vibration prediction of a flexible cylinder by three-dimensional strip model," *Ocean Eng.* **205**, 107318 (2020).
- ³⁴D. Deng, W. W. Zhao, and D. C. Wan, "Numerical study of vortex-induced vibration of a flexible cylinder with large aspect ratios in oscillatory flows," *Ocean Eng.* **238**, 109730 (2021).
- ³⁵M. S. Gritskevich, A. V. Garbaruk, J. Schutze *et al.*, "Development of DDES and IDDES formulations for the $k-\omega$ shear stress transport model," *Flow, Turbul. Combust.* **88**, 431–449 (2012).
- ³⁶F. R. Menter, K. Martin, and L. Robin, "Ten years of industrial experience with the SST turbulence model," *Turbul. Heat Mass Transfer* **4**(1), 625–632 (2003).
- ³⁷B. W. Fu, L. Zou, and D. C. Wan, "Numerical study of vortex-induced vibrations of a flexible cylinder in an oscillatory flow," *J. Fluids Struct.* **77**, 170–181 (2018).
- ³⁸Y. Bao, R. Palacios, M. Graham *et al.*, "Generalized thick strip modelling for vortex-induced vibration of long flexible cylinders," *J. Comput. Phys.* **321**(800), 1079–1097 (2016).
- ³⁹R. W. Clough and J. Penzien, *Dynamics of Structures*, 3rd ed. (Computers & Structures, Inc., 2003).
- ⁴⁰E. Lehn, *VIV Suppression Tests on High L/D Flexible Cylinders* (Norwegian Marine Technology Research Institute, 2003).
- ⁴¹H. Park, R. A. Kumar, and M. M. Bernitsas, "Suppression of vortex-induced vibrations of rigid circular cylinder on springs by localized surface roughness at $3 \times 10^4 \leq \text{Re} \leq 1.2 \times 10^5$," *Ocean Eng.* **111**, 218–233 (2016).
- ⁴²H. Hu, Z. H. Wei, and D. C. Wan, "Numerical analysis of vortex-induced vibration suppression of a flexible riser attaching with symmetric strips," in *Proceedings of the 32nd International Ocean and Polar Engineering Conference*, Shanghai, China, 2022.